Benchmark exercise on image-based permeability determination of engineering textiles: Microscale predictions

Elena Syerko, Tim Schmidt, David May, Christophe Binetruy, Suresh G. Advani, Stepan Lomov, Luisa Silva, Sergey G. Abaimov, Nesrine Aissa, Iskander S. Akhatov, et al.

Benchmark exercise on image-based permeability determination of engineering textiles: microscale predictions

E. Syerko[1]*, T. Schmidt[2], D. May[2], C. Binetruy[1,3], S.G. Advani[3,1], S. Lomov[4,5], L. Silva[1], S. Abaimov[5], N. Aissa[1], I. Akhatov[5], M. Ali[6], N. Asiaban[7], G. Broggi[8], J. Bruchon[9], B. Caglar[8], H. Digonnet[1], J. Dittmann[10], S. Drapier[9], A. Endruweit[12], A. Guilloux[13], R. Kandinskii[4], A. Leygue[1], B. Mahato[5], P. Martínez-Lera[14], M. Matveev[12], V. Michaud[8], P. Middendorf[10], N. Moulin[9], L. Orgéas[11], C.H. Park[15], S. Rief[16], M. Rouhi[17,18], I. Sergeichev[5], M. Shakoor[15], O. Shishkina[14], Y. Swolfs[4], M. Tahani[7], R. Umer[6], K. Vanclooster[14], R. Vorobyev[5]

[1]Nantes Université, Ecole Centrale Nantes, CNRS, GeM, UMR 6183, Nantes, F-44000, France

[2]Leibniz-Institut für Verbundwerkstoffe GmbH, Erwin-Schrödinger-Straße, Geb. 58, 67663 Kaiserslautern, Germany

[3]University of Delaware, Department of Mechanical Engineering, 126 Spencer Lab, DE 19716 Newark, USA

[4]KU Leuven, Department of Materials Engineering, Kasteelpark Arenberg 44, 3001 Leuven, Belgium

[5]Skolkovo Institute of Science and Technology, Center for Materials Technologies, Bolshoy Boulevard 30, Moscow, Russia

[6]Khalifa University of Science and Technology, Department of Aerospace Engineering, Abu Dhabi, United Arab Emirates

[7]Ferdowsi University of Mashhad, Department of Mechanical Engineering, Mashhad, Iran

[8]Ecole Polytechnique Fédérale de Lausanne (EPFL), Laboratory for Processing of Advanced Composites (LPAC), Institute of Materials (IMX), Station 12, 1015 Lausanne, Switzerland

[9]Mines Saint-Étienne, Univ. Lyon, CNRS, UMR 5307 LGF, 158 Cours Fauriel 42023, Saint-Étienne, France

[10]University of Stuttgart, Institute of Aircraft Design, Pfaffenwaldring 31, 70569 Stuttgart, Germany

[11]Univ. Grenoble Alpes, CNRS, Grenoble INP, 3SR Lab, 38000 Grenoble, France

[12]University of Nottingham, Faculty of Engineering, Jubilee Campus, Nottingham, NG8 1BB, UK

[13]TENSYL, 48 rue Jacques de Vaucanson, Pôle Arts & Métiers, 17180 Périgny, France

[14]Siemens Industry Software NV, Interleuvenlaan 68, 3001 Leuven, Belgium

[15]IMT Nord Europe, Institut Mines-Télécom, Univ. Lille, Center for Materials and Processes, F-59000 Lille, France

[16]Fraunhofer-Institut für Techno- und Wirtschaftsmathematik (ITWM), Fraunhofer-Platz 1, Kaiserslautern, D-67663, Germany

[17]RISE Research Institutes of Sweden, Division Materials and Production - RISE SICOMP AB, Box 104, SE-431 22, Mölndal, Sweden

[18]National University of Singapore (NUS), Department of Mechanical Engineering, Faculty of Engineering, 9 Engineering Drive 1, Singapore 117576, Singapore

*Corresponding author. Tel.: + 33 2 40 37 16 96
E-mail address: elena.syerko@ec-nantes.fr

Abstract

Permeability measurements of engineering textiles exhibit large variability as no standardization method currently exists; numerical permeability prediction is thus an attractive alternative. It has all advantages of virtual material characterization, including the possibility to study the impact of material variability and small-scale parameters. This paper presents the results of an international virtual permeability benchmark, which is a first contribution to permeability predictions for fibrous reinforcements based on real images. In this first stage, the focus was on the microscale computation of fiber bundle permeability. In total 16 participants provided 50 results using different numerical methods, boundary conditions, permeability identification techniques. The scatter of the predicted axial permeability after the elimination of inconsistent results was found to be smaller (14%) than that of the transverse permeability (~24%). Dominant effects on the permeability were found to be the boundary conditions in tangential direction, number of sub-domains used in the renormalization approach, and the permeability identification technique.

Keywords: A. Fabrics/textiles **A.**Tow **B.**Permeability **C.**Computational modeling **E.**Resin flow

---

1 Introduction

Liquid Composite Molding (LCM) processes are used to produce fiber-reinforced polymer composites. In all LCM processes, dry fiber preforms are placed in a mold and are impregnated with a resin, typically thermoset. In addition to a complete impregnation, the fastest possible impregnation is also desirable for economic reasons. For this purpose, filling simulations are used to design and optimize LCM processes to reduce air entrapment and accelerate impregnation [1-4]. However, the accuracy of the filling simulations is governed by the input data characterizing the material and the process. Darcy's law [5] relates the volume-averaged flow velocity of the resin $\underline{v}$ to the pressure gradient $\nabla \underline{p}$ and the gravitational contribution $\rho \underline{g}$ (ρ is the resin density), dynamic resin viscosity μ, and the permeability tensor $\boldsymbol{K}$ of the fibrous preform:

$$\underline{v} = \frac{1}{\mu} \boldsymbol{K} \cdot \left(-\nabla \underline{p} + \rho \underline{g} \right). \tag{1}$$

The permeability tensor $\boldsymbol{K}$ that quantifies the hydraulic capability of the fibrous structure to be impregnated is a crucial material parameter to address the resin flow. Permeability is usually determined experimentally to get the input values for LCM simulations. An extensive experimental test program must be carried out to find permeability values that account for different fiber volume fractions, shear angles, and other variations in the material. However, for economic reasons, simplifications are often made with the aim to reduce the test program. In addition to these simplifications, it is worth to note that the experimental characterization of permeability is not standardized yet. Several benchmark studies have

shown that this can result in variations of more than 20% for the experimental determination of permeability [6-11].

While filling simulations of LCM processes at component level are already established [1-3], the status is quite different in the field of material characterization, especially for permeability determination. Today, the numerical permeability prediction is mainly addressed by the scientific community [12-19]. Nevertheless, with improved methods for permeability prediction and the increasing computing power, the potential of numerical methods is also increasing. Through virtual permeability prediction:

- permeability can be determined without generating large amounts of material waste (textiles, testing fluid, other consumables) and without using elaborate equipment;
- influencing factors can be investigated, which cannot be studied experimentally or require a considerable effort;
- large parametric studies can be carried out efficiently;
- Intrinsic understanding of flow in textiles or textile stacks can provide a path for process optimization.

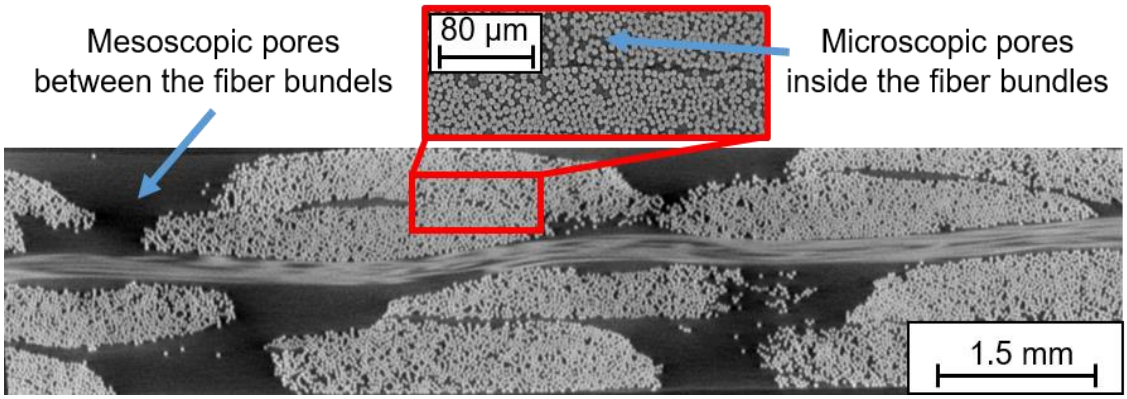

Figure 1: Multiscale pore structure of fibrous textiles

The virtual permeability prediction offers great potential but is not without its numerous challenges due to the complex structure of fiber reinforcements. These include multiscale porosity, anisotropic structure, and multiple spatial variations. Due to multiscale porosity, it is reasonable to use multiscale approaches for virtual permeability prediction. For the permeability prediction, usually the microscopic and mesoscopic scale are explored, whereas the macroscale influence is needed in the filling simulations. Fig. 1 provides the distinction between the microscale (fiber scale, µm-range) within fiber bundles, the mesoscale (textile scale, mm-range) and the macroscale (component scale, cm to m-range). On the other hand, a large number of numerical methods and influencing parameters [12-18,20,21], as well as their significant effects on the numerical permeability prediction, is the main cause for the lack of acceptance of the numerical results. In order to establish confidence in numerical

permeability predictions, it is important to define guidelines to prevent errors. Therefore, the virtual permeability benchmark (VPB) was launched with the aim to (1) benchmark currently used methods and tools for virtual permeability predictions, (2) identify sources of possible variations and errors, and (3) develop guidelines for numerical prediction of permeability of engineering textiles. No specific conditions for the permeability calculation methods were imposed to the participants for this first numerical benchmark exercise to get a complete overview of the available techniques and compare their impact on the permeability prediction.

The first step of the benchmark study is focused on the microscopic scale. The results are presented and discussed in this paper. This benchmark was organized by the Research Institute in Civil Engineering and Mechanics (GeM) of Ecole Centrale de Nantes (ECN, Nantes, France) and Leibniz-Institut für Verbundwerkstoffe GmbH (IVW, Kaiserslautern, Germany), and supported by KU Leuven (Belgium) and University of Delaware (USA) as members of the Advisory Board. Table 1 lists the research groups involved in the VPB (the order of the list does not correspond to the numbering of the results).

Table 1: LIST OF PARTICIPANTS*

Institution / Department	Country
KU Leuven / Department of Materials Engineering, Composite Materials Group	Belgium
Siemens Industry Software NV	Belgium
Nantes Université, Ecole Centrale Nantes / High Performance Computing Institute (ICI)	France
Nantes Université, Ecole Centrale Nantes – CNRS / Research Institute in Civil Engineering and Mechanics (GeM)	France
Mines Saint-Etienne, Université Lyon – CNRS / LGF	France
IMT Nord Europe / Center for Materials and Processes	France
TENSYL	France
Fraunhofer Institute for Industrial Mathematics (ITWM)	Germany
Leibniz-Institut für Verbundwerkstoffe GmbH	Germany
University of Stuttgart / Institute of Aircraft Design	Germany
Ferdowsi University of Mashhad National University of Singapore RISE Research Institutes of Sweden	Iran Singapore Sweden
Skolkovo Institute of Science and Technology / Center for Design, Manufacturing and Materials	Russia
Skolkovo Institute of Science and Technology / Center for Design, Manufacturing and Materials	Russia
Ecole Polytechnique Fédérale de Lausanne / Laboratory for Processing of Advanced Composites (LPAC) Université Grenoble Alpes – CNRS / Laboratory Soils, Solids, Structures, Risks (3SR Lab)	Switzerland France
University of Nottingham / Composites Research Group, Faculty of Engineering	UK
Khalifa University of Science and Technology	United Arab Emirates

*The order of participants does not correspond to the numbering of the results given hereafter.

2 Materials & Data Preparation

A microscopic volume (MSV) of the fiber tow (fibers nominal diameter 9 µm) extracted from an X-ray microscope scan (voxel size 0.521^3 µm^3) of the twill-weave fiber glass reinforced composite (Fig. 2) was provided to the participants of the benchmark for the determination of its permeability tensor. The MSV is available on the repository at https://doi.org/10.5281/zenodo.6611926. To avoid an additional source of variation originating from the image processing, a binarized volume with the fibrous phase already segmented from the matrix phase was used. Detailed information on the material of the sample, its preparation, imaging, and segmentation procedure is provided in the Supplementary material.

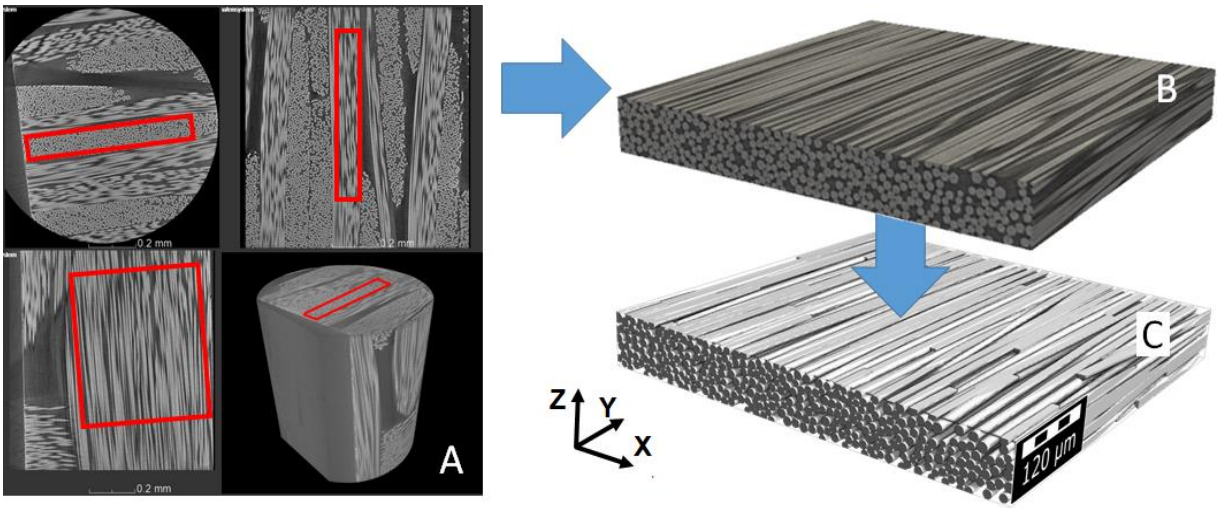

Figure 2: 3D X-ray microscope scan from a section of the cut-out (A), extracted gray-scale non-segmented MSV (B), and segmented MSV for calculation (C)

3 Methods

In total, 16 benchmark participants (Table 1) submitted around 50 results of permeability calculation with auxiliary additional studies on sub-domains, mesh refinement, boundary conditions (BC), and analytical estimations. Table 2 summarizes models, numerical methods, discretization schemes, and other parameters used by the participants to run the simulations. Three participants (#2, #6, and #14) performed calculations in 2D on 2D cross-sections cut transverse to the fiber direction and, therefore, only obtained permeability values transverse to the fibers. All other participants solved the problem in 3D.

The majority of participants used the finite volume method (FVM) for the numerical resolution. Two participants used the finite difference method (FDM): either in its conventional form (#8), or using the explicit-jump immersed interface method (#16), which can handle the local properties discontinuities [22]. One participant (#4) applied the control-

volume based finite-element method (CVFEM); and the remainder used the finite element method (FEM).

The voxel-based discretization was employed either in the classical way – one element per voxel, or with a locally coarsened / refined mesh by the LIR-tree approach [23], which is a generalization of the Octree. Whenever both element-per-voxel and LIR-tree discretization were tested by a participant it is indicated as "*Voxel-based / LIR*" in Table 2. The voxel-based uniform mesh refinement was also applied by the participant #3. Two of the initial dimensions of their 900x100 domain were transformed into 1800x200, while in the third dimension (fiber direction) each 5 voxels were merged in 1 in order to compensate for the increase of degrees of freedom (DOFs) without affecting the computed permeability values, which was verified. Remeshing of the initial voxelized domain and geometry-based discretization was often used by the participants to decrease the number of DOFs, and thus the computational effort.

Table 2: Overview of numerical methods and model dimensions used for permeability calculation

Participant #	Numerical approximation	Discretization	Flow model	2D / 3D formulation	Physical variables formulation	Model size, voxels / Voxel size, μm^3	FVC, %
1	FVM	Voxel-based	Stokes	3D	SIMPLE	1003x973x124 / 0.521^3 μm^3	56.46
2	FEM	Geometry-based	Navier-Stokes	2D	mixed velocity-pressure	10 2D slices of ≈1003x124 / 0.521^3 μm^3	56.73 (55.06 – 59.54), 58.54 (57.08 – 61.39)
3	FVM	Voxel-based	Navier-Stokes	3D	mixed velocity-pressure	1800x180x200 / 0.2605 µm x 2.605 µm x 0.2605 µm	57.00
4	CVFEM	Voxel-based	Navier-Stokes	3D	mixed velocity-pressure	10 sub-volumes of ≈1003x100x124 for Kxx,Kzz 10 sub-volumes ≈100x973x124 for Kyy / 0.521^3 μm^3	56.46 (54.02 – 58.78), 56.46 (48.42 – 60.88)
5	FVM	Voxel-based - LIR	Stokes	3D	mixed velocity-pressure	1003x973x124 / 0.521^3 μm^3	56.46
6	FEM	Geometry-based	Stokes	2D	mixed velocity-pressure	973 2D slices of 1003x124 / 0.521^3 μm^3	55.87
7	FVM	Geometry-based	Navier-Stokes	3D	SIMPLE	1003x973x124 / 0.521^3 μm^3	59.87
8	FDM	Voxel-based	Stokes	3D	mixed velocity-pressure	972x972x108: 648 sub-volumes of 54x54x54 / 0.521^3 μm^3	57.16
9	FVM	Geometry-based	Stokes	3D	mixed velocity-pressure	16 sub-volumes of ≈251x243x124 / 0.521^3 μm^3	56.36 (46.96 – 60.84)
10	FEM	Voxel-based	Stokes	3D	pseudo-compressibility (penalization)	64 sub-volumes of ≈126x122x124 / 0.521^3 μm^3	56.46 (46.49 – 61.81)
11	FVM	Geometry-based	Navier-Stokes	3D	mixed velocity-pressure	1003x679x124 / $\approx 0.7368^3$ μm^3	58.69
12	FVM	Voxel-based / LIR	Stokes	3D	SIMPLE mixed velocity-pressure	1003x973x124 / 0.521^3 μm^3	56.46
13	FVM	Geometry-based	Navier-Stokes	3D	mixed velocity-pressure	124x192x124 / 0.521^3 μm^3	59.54
14	FEM	Geometry-based	Stokes	2D	mixed velocity-pressure	973 2D slices of 1003x124 / 0.521^3 μm^3	56.46, 55.57
15	FEM	Geometry-based	Stokes	3D	mixed velocity-pressure	1003x973x124 / 0.521^3 μm^3	56.46, 51.00
16	FVM FDM	Voxel-based / LIR	Stokes	3D	SIMPLE mixed velocity-pressure	1003x973x124 / 0.521^3 μm^3 10 sub-volumes ≈1003x100x124 / 0.521^3 μm^3	56.46, 56.46 (54.02 – 58.78)

The majority of the participants naturally used the Stokes flow model. It should be noted that for the determination of permeability of the porous medium only the Stokes equation is convenient to address the creeping flow condition. If the Navier-Stokes equations are nevertheless used, the local Reynolds number of the flow through the pores must meet the condition $Re << 1$.

The mixed velocity-pressure formulation was the most used one in the benchmark, compared to the SIMPLE and pseudo-compressibility formulations. The latter, whose advantage is a reduction of the number of DOFs in the computation because only the velocity field without pressure is solved, was only used by the participant #10.

In addition to in-house developed codes, commercially available software either for flow computation, or permeability calculation were used by some participants:

- Ansys CFX®, Fluent® by Ansys;
- FlowTex® by KU Leuven;
- FlowVision® by TESIS Ltd;
- GeoDict® by Math2Market;
- OpenFOAM® by OpenCFD Ltd;
- Simcenter™ 3D Thermal/Flow solution by Siemens Digital Industries Software;
- Zébulon® by Z-set.

Some of these software were employed by several participants, but with different applied conditions and input parameters.

Participants #2 and #14 also provided results computed on images they segmented themselves (results #2b and #14b): therefore, two different values of the resulting fiber volume content (FVC), which is a ratio of the volume of fibers to the total volume, are reported for each of these participants in Table 2. Different ranges of the FVC are also shown in Table 2 if the computations were done on a set of sub-volumes, as the local FVC can vary significantly due to the non-uniform distribution of twisted fibers, or local compaction at the warp/weft cross-over.

For some of the presented computational techniques only the computation on the sub-volumes or on a set of 2D slices of the whole domain was possible: not only due to limitation in computational time, but often because of memory constraints. For instance, memory limitations were reported for the solvers used by #4 and #8. The technical characteristics of the computational resources used and simulation times for all results of the benchmark are summarized in Table 2 in the Supplementary material. The computational speed and hence the efficiency of the methods used cannot be compared as they were implemented on computers with different performance, parallelized in different ways, even if these parameters were normalized by the number of DOFs used in each model.

The different boundary conditions in flow and tangential to flow directions implemented by the participants in simulations are summarized in Table 3 and schematized in Fig. 3. Their influence on the permeability prediction is discussed in the following sections.

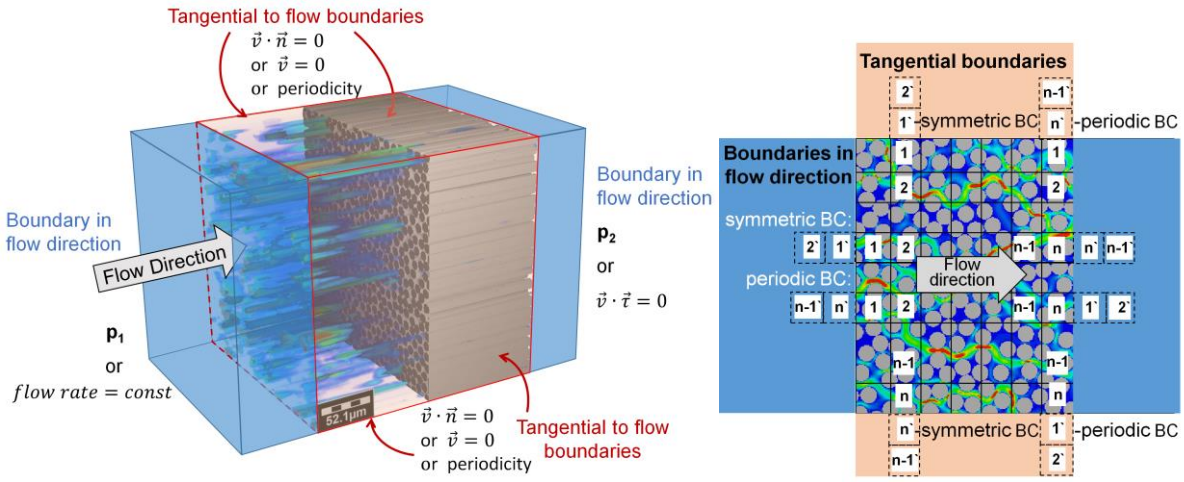

Figure 3: Scheme of different types of boundary conditions for velocity and pressure in flow and tangential to flow directions

In the flow direction a constant pressure gradient or a constant flow rate was imposed. At the tangential boundaries to the flow (Fig. 3) conditions of symmetry, translational periodicity, or no-slip were imposed. The difference between symmetric and periodic BC is illustrated in Fig. 3. All scalar quantities (pressure, velocity components) in the ghost cells/nodes (*1`,2`,…,n`*) are obtained from the corresponding physical cells/nodes (*1,2,…,n*). For instance, in case of periodic BC cell/node *n`* corresponds to the cell/node at the opposite periodic boundary *n*.

Table 3: Boundary conditions used by each participant

Participant #	BC in flow direction	Inflow/outflow regions, µm (voxels)	BC in tangential direction
1	fixed pressure	50,02 µm (96 voxels)	periodic
2	free (Lagrange multiplier)	-	symmetric **v** • **n** = 0 (Lagrange multiplier)
3	fixed pressure	-	periodic v
4	fixed pressure	-	symmetric **v** • **n** = 0
5	fixed pressure	20,84 µm (40 voxels)	symmetric
6	fixed pressure	-	symmetric **v** • **n** = 0
7	fixed pressure	-	no-slip **v** = 0
8	fixed pressure	-	periodic v
9	fixed pressure	-	symmetric **v** • **n** = 0
10	fixed flow rate on inlet, **v** • **τ** = 0 on outlet	7,8 µm (15 voxels)	symmetric **v** • **n** = 0
11	fixed pressure	-	no-slip **v** = 0
12	fixed pressure	5,2 µm (10 voxels)	12a,12c: periodic; 12b,12d: symmetric
13	fixed pressure	-	symmetric **v** • **n** = 0
14	fixed pressure	-	no-slip **v** = 0
15	fixed pressure	-	symmetric **v** • **n** = 0
16	fixed pressure	5,2 µm (10 voxels)	periodic, except 16b where: symmetric

The inflow / outflow regions, used by some participants, are fluid-only zones artificially added to the initial domain's inlet and/or outlet upstream and downstream. In general, they serve to prevent a non-periodic structure from becoming non-percolating in the cases when translational periodicity is imposed in the flow direction [24]. They also allow the flow to be fully developed at the inlet and outlet of the initial domain, which is particularly important for low-porosity structures. It should be noted that in Table 2 the model size is indicated without taking into account a possible presence of inflow / outflow regions in the computations. In Table 3 the length of regions is given per region at each side: upstream and downstream.

4 Results and discussion

4.1 Overview

Fig. 4 presents the diagonal permeability components K_{xx}, K_{yy}, K_{zz} (for the segmented MSV in Fig. 2) of all reported results. Naturally, one can see higher values of the axial permeability K_{yy} in Fig. 4 compared to the transverse permeability components K_{xx} (tow in-plane dimension) and K_{zz} (tow thickness direction) as fiber tows are transversely isotropic. An attempt was made to choose the MSV orientation so that the flow principal directions across the structure were aligned with the MSV *Oxyz* axis. The off-diagonal components of the permeability tensor would be expected in this case to be equal or very close to zero. However, there may be an impact from the fact that the MSV does not contain the complete twist period of the tow (due to the computational limitations), though it is a very slight twist. In the case of such an influence, the principal flow directions will not be aligned with the MSV *Oxyz* axis, and thus the off-diagonal components of the permeability tensor will reflect this. The question about the off-diagonal terms is discussed in detail in Section 4.5.

A larger scatter of values can be observed for the transverse permeability than for the axial one. Two participants also made analytical estimations based on models in [25-27] – results #4b, #4c, and #7b. The discussion about these estimations can be found in the Supplementary material. Without the analytical results, the coefficient of variation C_v of the axial permeability is 81%, while it is 137% and 119% for the transverse permeabilities K_{xx} and K_{zz} respectively. The C_v is defined as a ratio between the standard deviation of the values and their arithmetical mean.

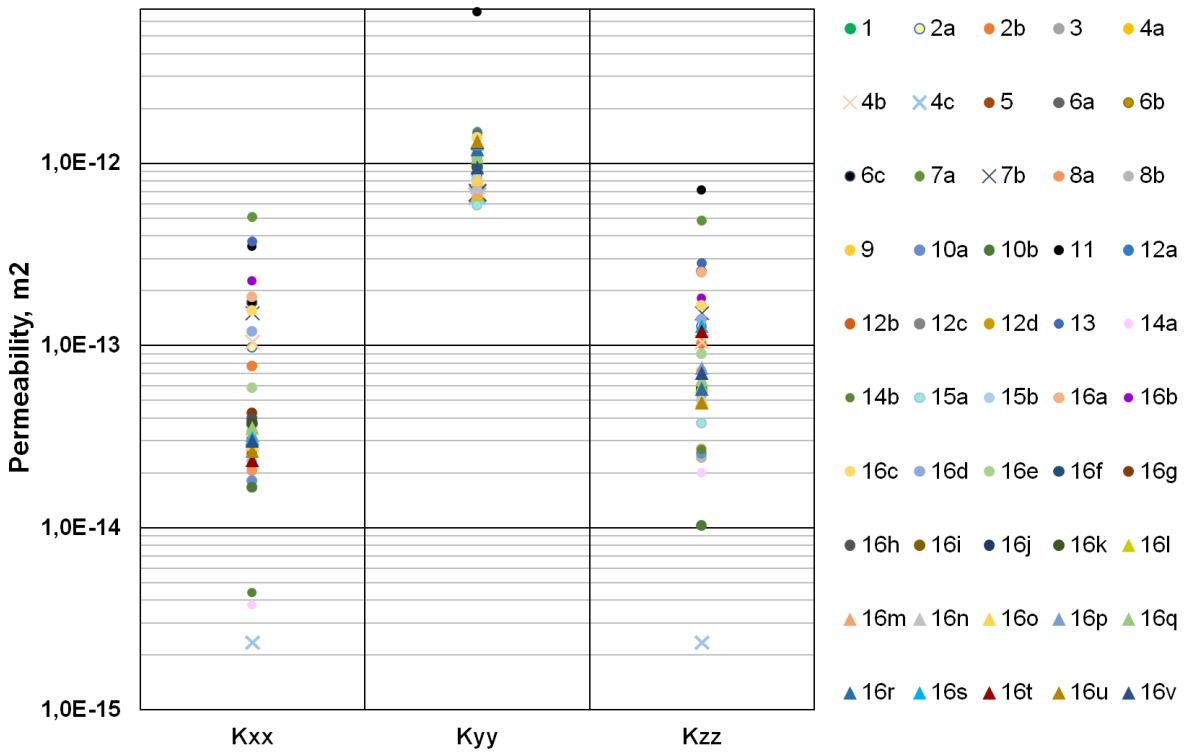

Figure 4: Overview of all reported permeability results: transverse K_{xx}, K_{zz} and axial K_{yy}. Analytical predictions are marked by 'x'

As already mentioned, some participants provided several results by varying some parameters or conditions:

- Results #6a-c differ between each other by the permeability calculation procedure, but are based on the same flow fields computed on 2D slices. The results based on 2D computations will be discussed in detail later on.
- Results #8a-b were computed on the same 3D sub-volumes but by two different permeability determination procedures, which are detailed in the following sections.
- Results #10a-b were both computed by the same method, however, the values #10a were calculated for the whole volume by averaging the values obtained by splitting the domain into 8 x 8 almost cubic sub-volumes, while the full permeability tensor #10b was calculated for the $1/10^{th}$ sub-volume of the whole domain with a slightly different fiber volume fraction.
- Results #12a-b used the same numerical methodology with voxel-based discretization, but different BC in the tangential direction: periodic or symmetric; while #12c-d used another numerical methodology with LIR-tree discretization and also varied BC in the tangential direction.
- Permeability values #15a and #15b were calculated by the same numerical method, however, #15b was computed on a virtually generated microstructure aimed at

reproducing the benchmark sample. The details on this virtual microstructure are given in the next section.

- Results #16a,c,d,e were calculated by the same explicit-jump immersed interface solver but with a modified tolerance of the permeability-based stopping criterion. Permeability values #16f-h were obtained with the help of the finite-volume solver that uses the LIR-tree discretization by also varying tolerances, while the values #16i-k – with a different finite-volume solver using the SIMPLE scheme and variable tolerances. Results #16l-u correspond to 10 sub-volumes, into which the whole domain was subdivided (Fig. 9). The result #16v was obtained by averaging the values #16l-u from the sub-volumes with harmonic and arithmetic means. Results #16a and #16b differ only by the boundary conditions imposed in the tangential directions: only #16b among all results #16 used symmetric BC, the others used periodic ones in order to reduce the computational cost.

4.2 Axial permeability

The coefficient of variation for the axial permeability values is smaller than that for the transverse permeability components. Fig. 5 shows all reported K_{yy} values, except those predicted analytically. The results based on the 2D formulation are not plotted in Fig. 5 as they were all computed on 2D cross-sections perpendicular to fiber direction and thus do not include the axial permeability component.

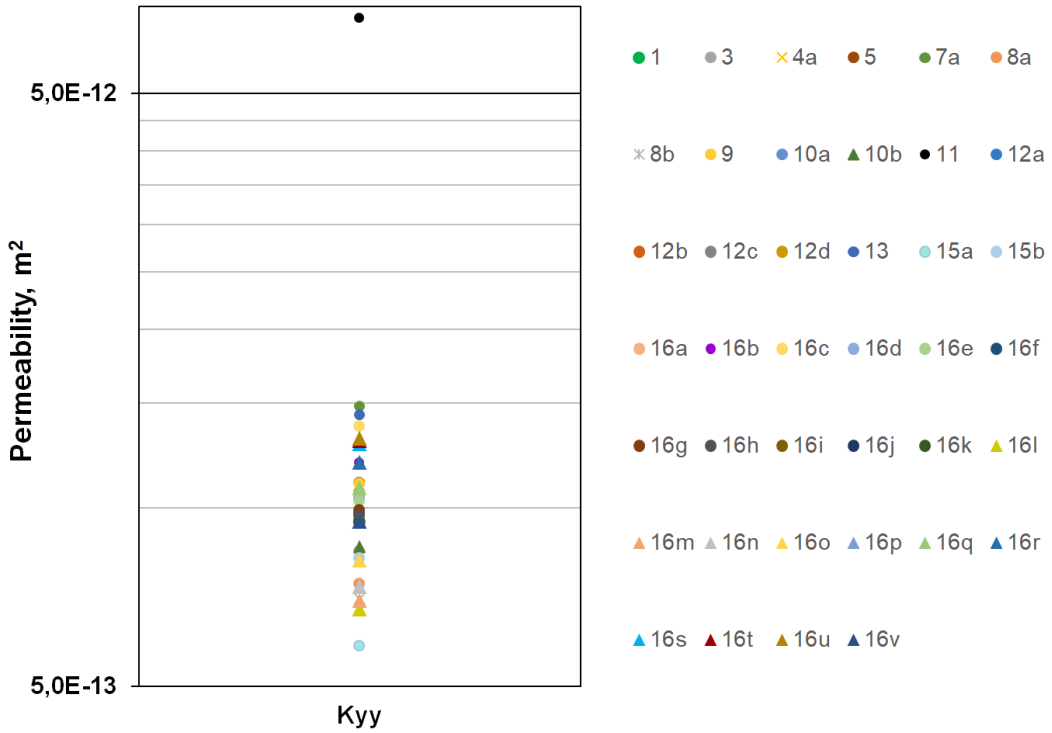

Figure 5: Axial permeability K_{yy} results (without the analytically predicted ones)

Value #11 stands out from the other results. The numerical domain of the simulation #11 was generated by extruding a 2D slice of the initial domain, thus without reproducing the

fibers misalignment. Besides, the originally given dimensions and resolution of the sample were not respected: they were higher in #11 (see Table 2). Therefore, #11 can be considered as an outlier. Without it, the coefficient of variation C_v of the axial permeability reduces from 81% to 21%, which is the order of magnitude of permeability variation reported for the experimental measurements [6-7] carried out on larger samples.

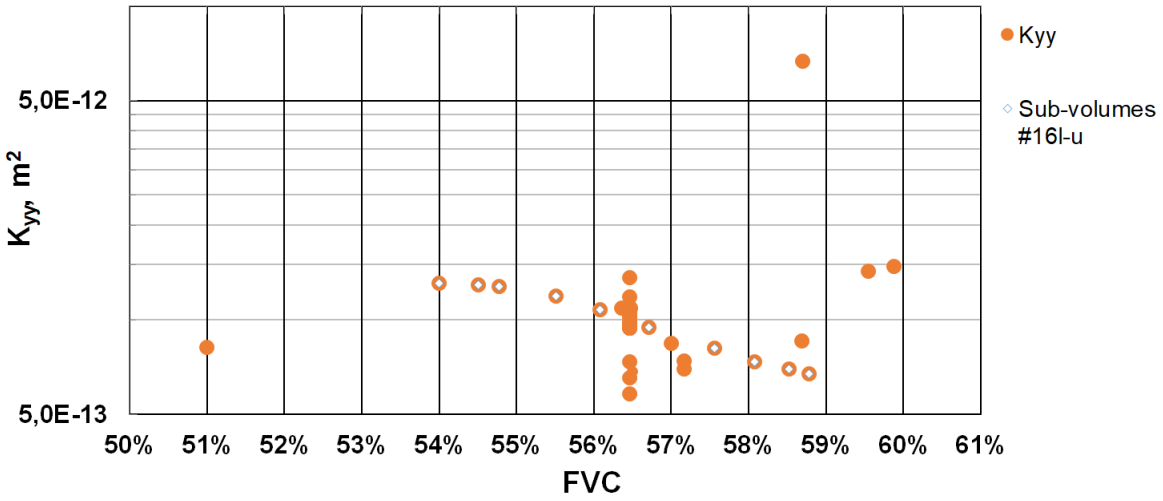

Figure 6: Correlation between the predicted axial permeability and fiber volume fraction

Fig. 6 shows the predicted axial permeability values versus the corresponding fiber volume fraction. The averaged FVC over the whole sample is 56.46%. However, locally there is a monotonic evolution of the FVC in the fiber direction (orientation of the tow) from 59% to 54% (Fig. 7), which can be explained by the compaction effects at the crossing of the fiber tows in the twill weave fabric.

The FVC also varies in the transverse direction, however, in a random manner: Fig. 8 shows 10 consecutive sub-volumes of the initial domain with the corresponding local FVC. Thus, results obtained on sub-domains of the initial domain may correspond to different FVCs. In summary, the reported FVC values different from 56.46% (Fig.6) can originate from:

- initial image domain subdivision into sub-domains;
- cropping of image edges;
- domain discretization method (e.g. if not voxel-based approach is used directly on the initial image, but a geometry-based remeshing).

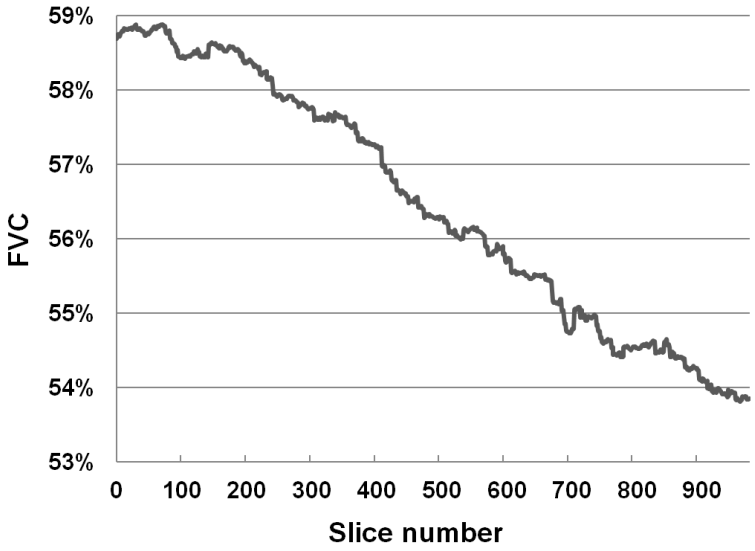

Figure 7: Evolution through 2D slices of the local FVC along the fiber direction

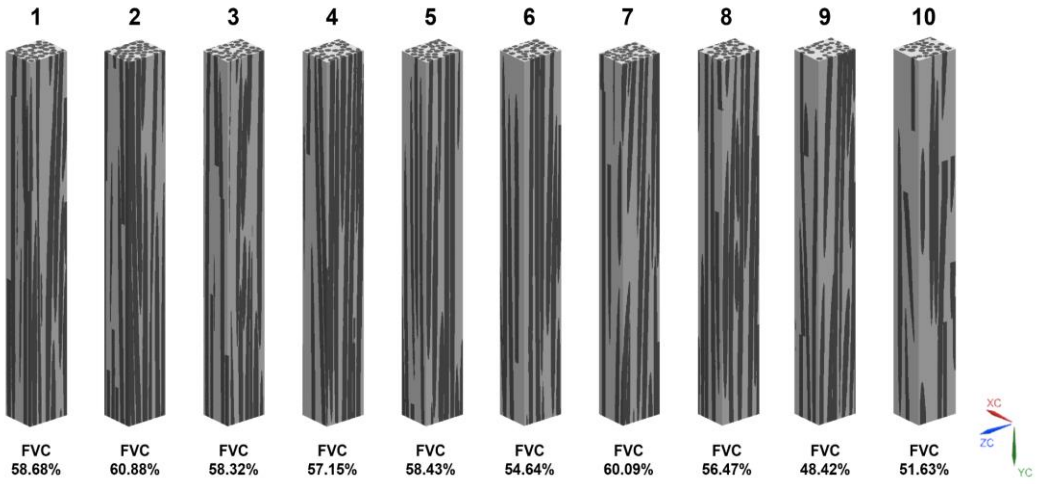

Figure 8: Domain sub-division (used in #4) into 10 sub-volumes cut along the fiber direction and corresponding evolution of the local FVC

The expected decrease of the permeability with increasing FVC is observed for the axial permeability in Fig. 6. The cluster of values at 56.46% has a C_v of 16%.

Few results deviate from the general trend. The result #15b obtained at 51% FVC corresponds to an optional exercise made by one of the participants to reproduce the real sample microstructure by the virtual generator with certain assumptions: parallel alignment of fibers and constant fiber diameter. It should be noted that this K_{yy} value at 51% FVC is lower than one would expect from a general trend, but higher than the value #15a obtained by the same technique at 56.46% FVC: K_{yy} = 5,84E-13 m^2, which is consistent. The question of the virtual idealized microstructure is considered in more detail in the Supplementary material.

Result #13 close to 60% in FVC can be partially explained by a very small size of the local domain – 2.5% of the initial image domain – taken for computation close to the sample

boundary with 59% FVC. Result #7a, also close to 60% in FVC, seems to be an outlier too as despite the computation over the whole image domain, it gave a higher permeability value than all values in the cluster and this is regardless a much higher FVC (apparently caused by the geometry-based remeshing). Due to the scaling mentioned above, the K_{yy} value #11 appears to be unrealistically high at such a high FVC. Without the outliers #7a, #11 and #13 the coefficient of variation of the axial permeability reduces to 20%. These results will not be included in the analysis of the axial permeability in the next sections.

4.2.1 Influence of cropping into sub-domains

Three types of results can be distinguished: i) those obtained from simulations on the entire image domain provided (18 results); ii) the ones recalculated for the whole domain that has been divided into sub-domains (6 results); iii) the ones obtained only on a part of the initial domain (11 results). If one considers only the results obtained or inferred for the whole volume (types i) and ii)), the C_v is reduced from 20% to 16%. If one restricts the results only to those of type i), the C_v reduces further but not by much to 15%. This finding suggests that in the case of axial permeability, to reduce memory resources, computing the local permeabilities on the sub-volumes and then deducing the permeability of the whole volume by averaging can provide a good approximation. It is also advantageous in terms of computational time because several smaller calculations can be run in parallel. However, with such a renormalization approach using the arithmetic and harmonic means the skew terms of the permeability tensor cannot be calculated. This is not problematic if the flow is computed in the principal directions in which case the skew terms are zero.

Participants #4, #9, #10, and #8 deduced the permeability for the whole volume from the values computed on the sub-volumes by dividing the domain into 10 (10x1), 16 (4x4), 64 (8x8), and 648 (18x18x2) sub-domains respectively. Participant #16 also provided an additional result #16v deduced from 10 sub-volumes cut transversely to the fiber direction (Fig. 9).

As the number of sub-volumes increases, there is a general trend for the permeability values to decrease as shown in Fig. 10. Thus, with an increase in the number of introduced sub-volume boundaries within the whole volume, the axial permeability tends to be underestimated. Results #16v and #8a are indicated by a lighter color in Fig. 10 since they slightly differ from the general trend.

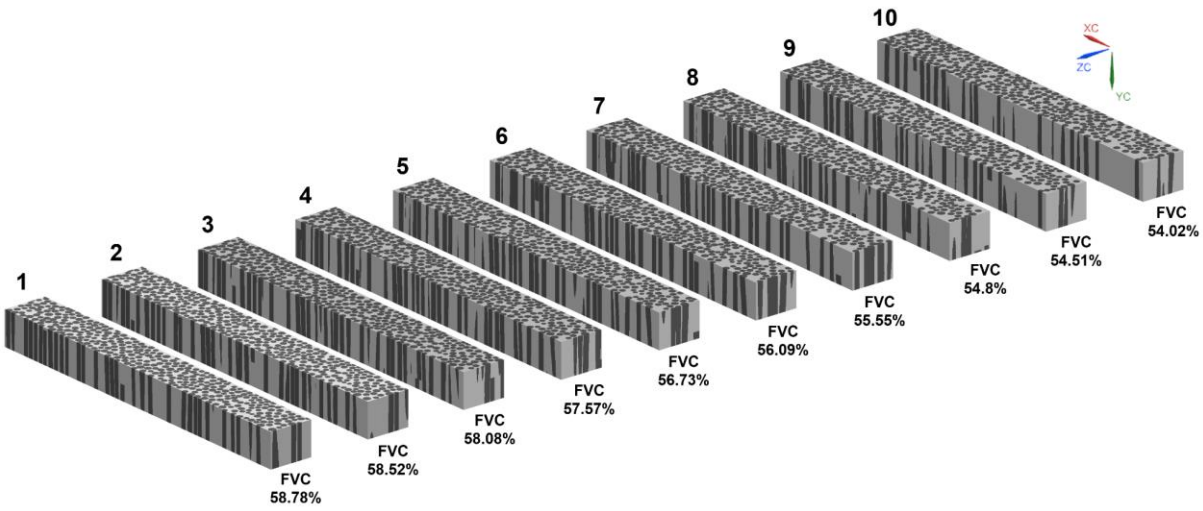

Figure 9: Domain sub-division (used in #4 and #16l-v) into 10 sub-volumes cut transversely to the fiber direction and corresponding evolution of the local FVC

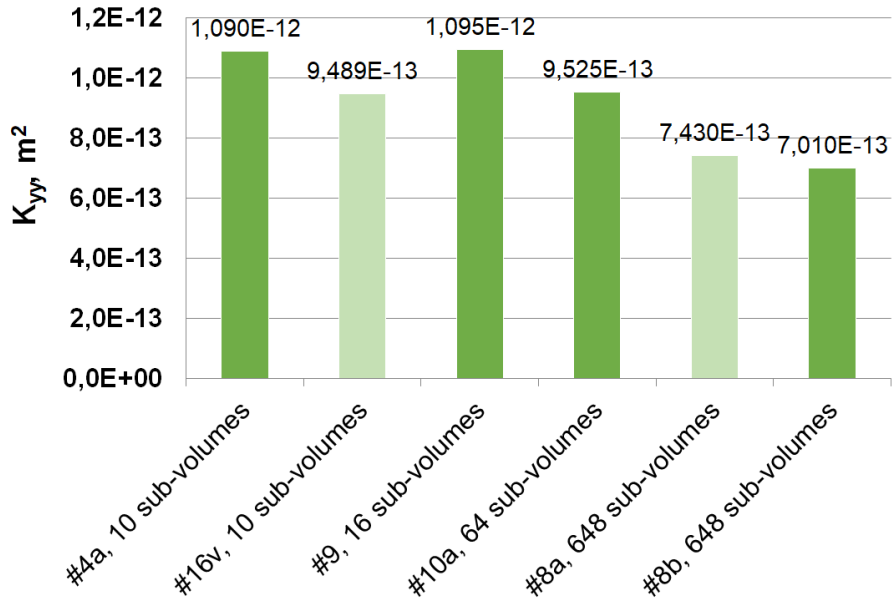

Figure 10: Axial permeability K_{yy} results #4a, #8a,b, #9, #10a, #16v computed by averaging the values from different number of sub-volumes

The value #8a is the result of a Darcy simulation over the whole volume with the distribution of permeabilities locally pre-computed on 648 sub-volumes taken as the input to the simulation; while all other results shown are obtained by the renormalization technique using arithmetic and harmonic means depending on the direction of the volume cropping. Apart from the different numerical methods used, the difference between #4a and #16v is the averaging by arithmetic mean over 10 sub-volumes shown in Fig. 8 in case of #4a, and by harmonic mean over 10 sub-volumes shown in Fig. 9 in case of #16v. This may not be the reason for such correlation between #16v and other values. It can originate from a

superposition of multiple factors at the same time: numerical scheme, BC, permeability identification procedure, etc.

Participant #3 also investigated the impact of increasing the size of the sub-domain taken in the middle of the whole sample on the permeability values in order to check whether a smaller domain size is sufficient to obtain permeability values close to those of the sample. However, no convergence of K_{yy} was observed with increasing domain size.

4.2.2 Influence of boundary conditions

The following BC were applied in the tangential direction by the participants (see Table 3): periodic (translational) BC, symmetric BC and no-slip BC. Since the results #7 and #11 will not be further analyzed, as explained earlier, and they used the no-slip BC, the impact of only periodic and symmetric BC in tangential direction is compared for the axial permeability (Fig. 11).

The geometry of the fiber bundle of the sample is not periodic in any direction. Some participants, however, used periodic BC in the tangential direction (#1, #3, #8, #12a,c, #16a,c-v) because it allows the development of transverse flow, unlike the other two types of boundary conditions. The presence of transverse flow in this case is particularly necessary for a correct determination of the full permeability tensor when the identification by Darcy's law is used for its calculation, taking into account the skew terms. If the symmetric BC is nevertheless applied, anisotropy effects that are not aligned with the principal flow directions will not be captured, and thus the skew terms of the permeability tensor obtained by Darcy's identification will not be correct (this point will be discussed in Section 4.5).

The disadvantage of symmetric BC is that the symmetry-based configuration [24] transforms the initial 3D computational domain into a domain four times larger. This results in longer simulation times, for example, in #16b, while compared to the same computation but with periodic BC in #16a: from 2 to 8 times longer, depending on the flow direction.

Only permeability values calculated or deduced (from sub-volumes) for the whole sample volume are compared in the following. In order to analyze the effect of boundary conditions without superimposing it on other influencing factors, it is relevant to compare results differing only by the applied BC, but using the same methods, discretization etc. (Fig. 11).

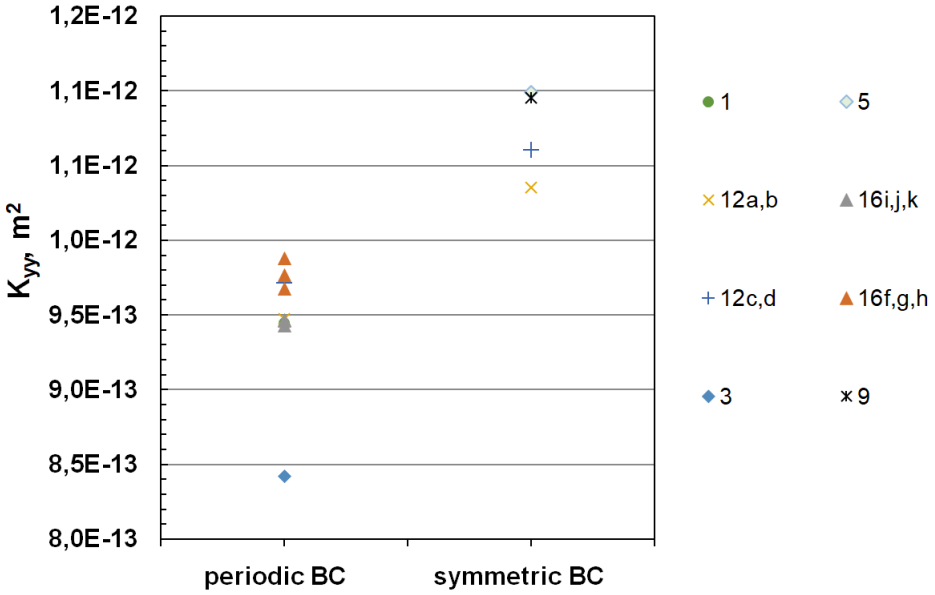

Figure 11: Axial permeability values calculated by the same methods but different boundary conditions in tangential direction: periodic and symmetric

One can see that the axial permeability values K_{yy} obtained with the symmetric boundary conditions are higher than the ones obtained with the periodic ones (Fig. 11). Results #12a,b, #12c,d, #16i,j,k, #16f,g,h are grouped in the graph as they rely on the same method, but have different residual tolerances or different BC. It should be noted that only participants #12a and #16i,j,k use exactly the same method and all conditions, and their results show an excellent match (with a given solution precision).

Results #1, #12a,b and #16i,j,k in Fig. 11 all use SIMPLE formulation of the Stokes equation, FVM numerical method, voxel-based discretization, and permeability calculation technique (Table 2). Their coefficient of variation is 4%, with the main difference coming from the different BC (periodic/symmetric) in #12a and #12b that differ between each other by 9%. The same mixed velocity-pressure formulation, FVM numerical method, LIR discretization, and permeability calculation technique, but different BC are also used by #5, #12c,d and #16f,g,h (Table 2): their C_v is 5%. Results of #3 and #9 were obtained using the same Navier-Stokes flow solver and permeability identification procedure, but different BC (periodic/symmetric) and different discretization (Table 2). Their relative difference is 26%.

If all results with periodic and symmetric BC in tangential direction are now analyzed all together, the trend revealed above is refuted by some results (Fig. 12). Indeed, as previously stated, the correlation of these results could be defined by multiple effects superimposed, not only by the boundary conditions. The #16a,c,d,e values were obtained by the explicit-jump immersed interface method that is known not to be adapted to the low-porosity structures [22], such as the material of the benchmark. The isolated position of #16c with

respect to other values can be attributed to its highest residual tolerance among the ones tested. The result #15a is also isolated.

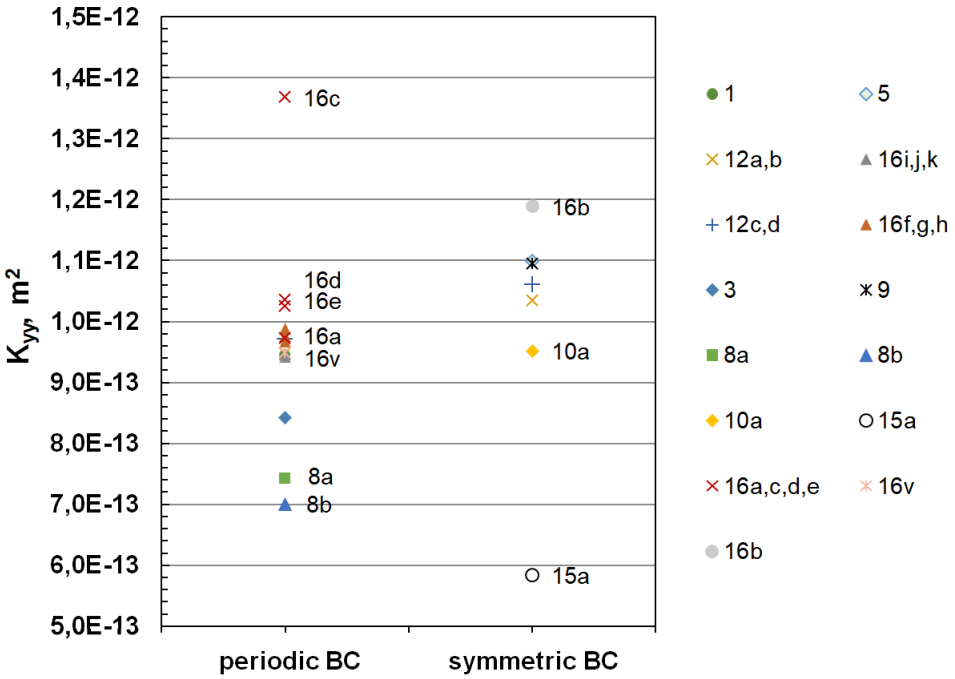

Figure 12: All axial permeability values calculated/deduced for the whole sample volume with periodic and symmetric boundary conditions in tangential direction

All participants imposed a pressure drop to compute the axial permeability, except for participant #10 who imposed a fixed flow rate at the inlet and the condition $\mathbf{v} \cdot \boldsymbol{\tau} = 0$ at the outlet (Table 3). Participants #1, #5, #10, #12, and #16 additionally used the inflow / outflow regions that have the advantage of allowing the use of periodic BC without a periodization procedure (by translation or by symmetry [24]) to apply on the sample. To investigate the effect of these regions on the permeability prediction separately, results that differ only by the length of these channels were selected. All other parameters and conditions in #5 and #12d were the same, except for this length, which was 40 voxels and 10 voxels respectively. Another pair of results from participants #1 and #12a also differ from each other only by the inflow / outflow regions with 96 and 10 voxels, respectively. The analysis of these values (see Supplementary material) showed that there is no apparent trend in permeability values with increasing length of these channels, or that their effect is dominated by other more influencing factors, such as the BC in tangential direction, for example.

4.3 Transverse permeability

Fig. 13 shows all reported values of K_{xx} and K_{zz}, except those predicted analytically. Results based on 2D computations are marked with stars. Despite the fact that fiber tows (in non-compacted state) are transversely isotropic media, higher values of the tow through-

thickness permeability component K_{zz} can be observed compared to the in-plane component K_{xx}, except for a few results: #7a, #10b, #13, and #16b.

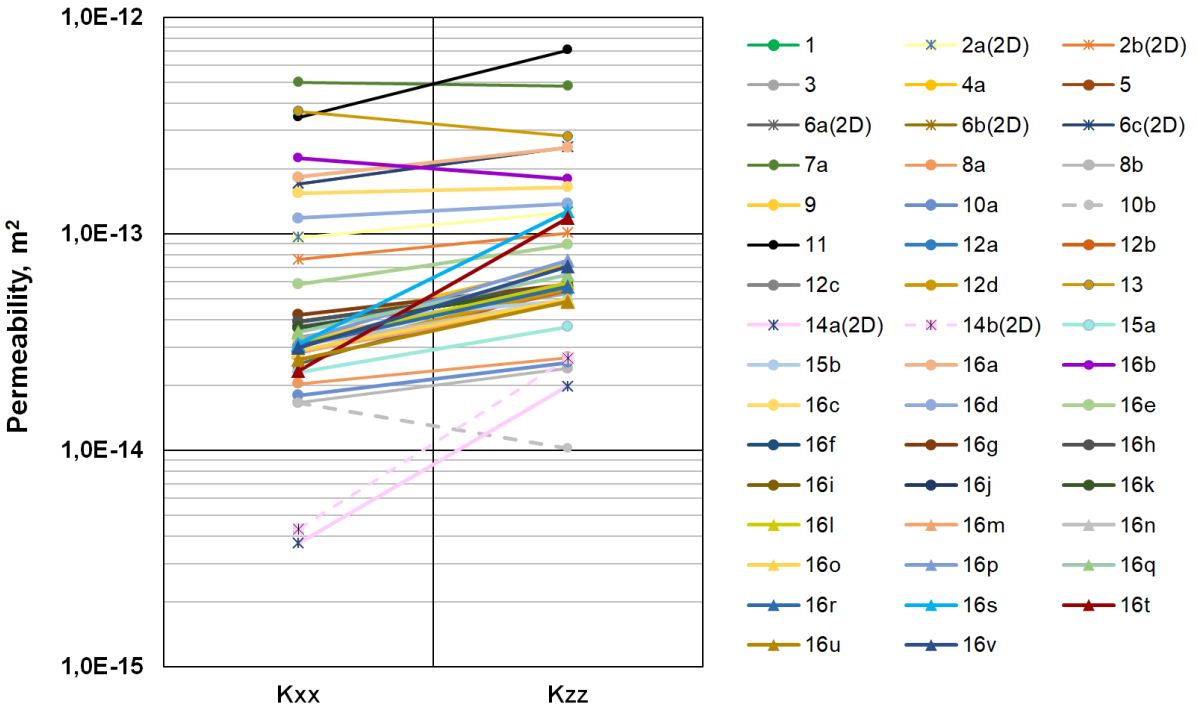

Figure 13: Transverse permeability K_{xx} and K_{zz} results (without analytically predicted ones). 2D computations are marked by 'x'

Result #10b is obtained for a sub-volume of size 1/10th of the full domain, cut in the fiber direction as shown in Fig. 8. The sub-volumes cut in this direction can have different local transverse anisotropy as they do not cover the whole width of the sample. This can explain the values #10b. Result #13 was also obtained on a very small sub-volume, as already explained in Section 4.2. On the contrary, results #7a and #16b were obtained on the whole sample and can, therefore, be considered as outliers: they will not be included in further analysis in the next sections. This confirms the previous conclusion regarding the axial permeability value in #7a. Concerning the result #16b, it was obtained by the explicit-jump immersed interface method, known not to be adapted to the low-porosity structures such as the material of the benchmark, where symmetric BC were applied in tangential directions, unlike other results #16.

Since the initially given domain dimensions and resolution were not respected in #11, as explained in Section 4.2, the values #11 will also be excluded from the analysis. Without results #7a, #10b, #11, #16b, and #13 the coefficient of variation of the transverse permeability reduces from 137% to 92% for K_{xx} and from 119% to 74% for K_{zz} with the mean values $\overline{K_{xx}}$ = 4,8E-14 m^2, $\overline{K_{zz}}$ = = 7,8E-14 m^2. It can be noted that the spread of K_{zz} values is smaller than that of the K_{xx} values. This can be partially attributed to a much smaller

dimension in the *Oz* direction, along which the flow is facilitated by a shorter flow extent than in the *Ox* direction.

Results #16c,a,d,e in this order use a decreasing tolerance: in Fig. 13 one can see how they monotonically approach the main cluster of results, except for result #16a which has higher values than #16c. Result #16a should be excluded from the analysis because apart from contradicting this monotonic trend in results #16c,a,d,e, it also shows a more pronounced anisotropy between the K_{xx} and K_{zz} values compared to the others (steeper slope in Fig. 13). Since #16c,d,e differ only by the tolerance of their stopping criterion, and #16d with an intermediate tolerance still differs from the cluster mean by 144% for the K_{xx} component, only the result #16e with the smallest tolerance should be considered in the analysis (K_{xx} of #16e differs from the mean by 20%).

We can also note a relatively high slope in Fig. 13 for the results #16s,t, as well as for #14a,b, i.e. a larger difference between the transverse permeability components. For the former, this can be explained by the fact that they were computed on the sub-volumes (these two results correspond to the low FVC). Results #14a,b are 2D results.

4.3.1 2D computation results

The aim of considering 2D computations is to analyze how close the permeability values predicted from cross-sections of 3D fiber bundle microstructures are to the full 3D solutions.

Participants #2, #6, and #14 calculated the permeability of the whole sample volume from calculations on a series of 2D slices orthogonal to the fiber direction, as shown in Fig. 4. All of them used a finite element method with a mixed velocity-pressure formulation and a geometry-based domain remeshing (Table 2). The difference between the results lies in the permeability calculation method, boundary conditions, number of slices taken for the computation (all slices in #6 and #14; 10 slices in #2) and the flow model used: results #2 were obtained by solving the Navier-Stokes equations, unlike the others.

No correlation between 2D and 3D results can be observed, 2D results spread over several decades (Fig. 13, 14). The coefficient of variation C_v of 2D results is large: 92% and 82% for K_{xx} and K_{zz} respectively. Interestingly, there is a significant difference between the values #6a and #6b,c (Fig. 14), which only differ from each other in the permeability identification method applied to the same flow fields computed on all 973 slices. Then the permeability was averaged over 973 slices in the same manner. From Fig. 13 it can be seen that results #6a, that used the identification method with Darcy's law without accounting for the anisotropy effects, are situated within the cluster of the 3D results, unlike other 2D predictions. Results #6b,c gave the full permeability tensor, while imposing its symmetry in #6c, and not in #6b. Results #2a,b are situated closer to the upper bound of the cluster of

results, while #14a,b tend to underestimate permeability, and particularly K_{xx} by a large amount.

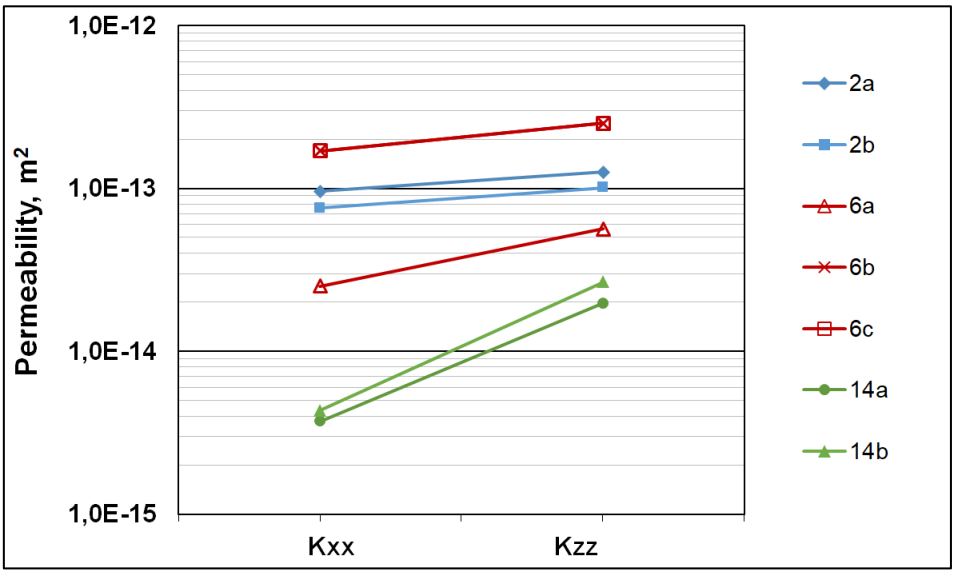

Figure 14: Transverse permeability K_{xx} and K_{zz} values obtained by 2D computations

Self-segmentation of images in #2b resulted in higher FVC (Table 2), and thus lower permeability values compared to #2a (Fig. 14), whereas the opposite occurred for the results #14a and #14b: the self-segmented 2D domains had lower FVC and thus higher permeability.

In #6a,b,c and #14a,b the permeability value for the whole sample volume was deduced by averaging the values of the 973 2D cross-sections; while in #2a,b 10 cross-sections uniformly distributed over the whole volume, starting from the first frontal slice, were used. In this way, the range of 54-59% FVC distributed along the fibers is roughly covered. On each of these 10 2D slices an average velocity was imposed for each direction and the average pressure gradient was calculated over the computed flow field. A least-square optimization method was then used to find the optimal components of the permeability tensor that allowed Darcy's law to fit the 20 velocity-pressure gradient solutions.

Considering the evolution of the local permeability across 10 slices uniformly distributed in the volume for results #6a and #14a,b (since #6b,c by the magnitude of their values are located far from the group of results), a monotonic decrease of the permeability with the FVC increase along the fibers can be observed especially for the K_{zz} component (Fig. 15b), but not for the K_{xx} component (Fig. 15a).

3D permeability values #16l-u and auxiliary values from #4a obtained over 10 sub-volumes oriented orthogonally to the fiber direction (Fig. 9) and containing 10 2D slices mentioned beforehand are also plotted in Fig. 15. Result #4a follows the same trend as the 2D results: transverse permeability K_{zz} decreases with increasing FVC, as does the axial permeability K_{yy} (see Fig. 6 in Section 4.2). Whereas its transverse permeability K_{xx} does not

show a decreasing trend, as if it was not influenced by the FVC (Fig. 15a). It can also be observed that the 3D results #16l-u do not show a monotonic decrease of K_{zz} with increasing FVC neither, unlike all other results in Fig. 15. This finding, therefore, questions the accuracy of the #16l-u values, as well as the one of the #16v result that was calculated from the #16l-u values.

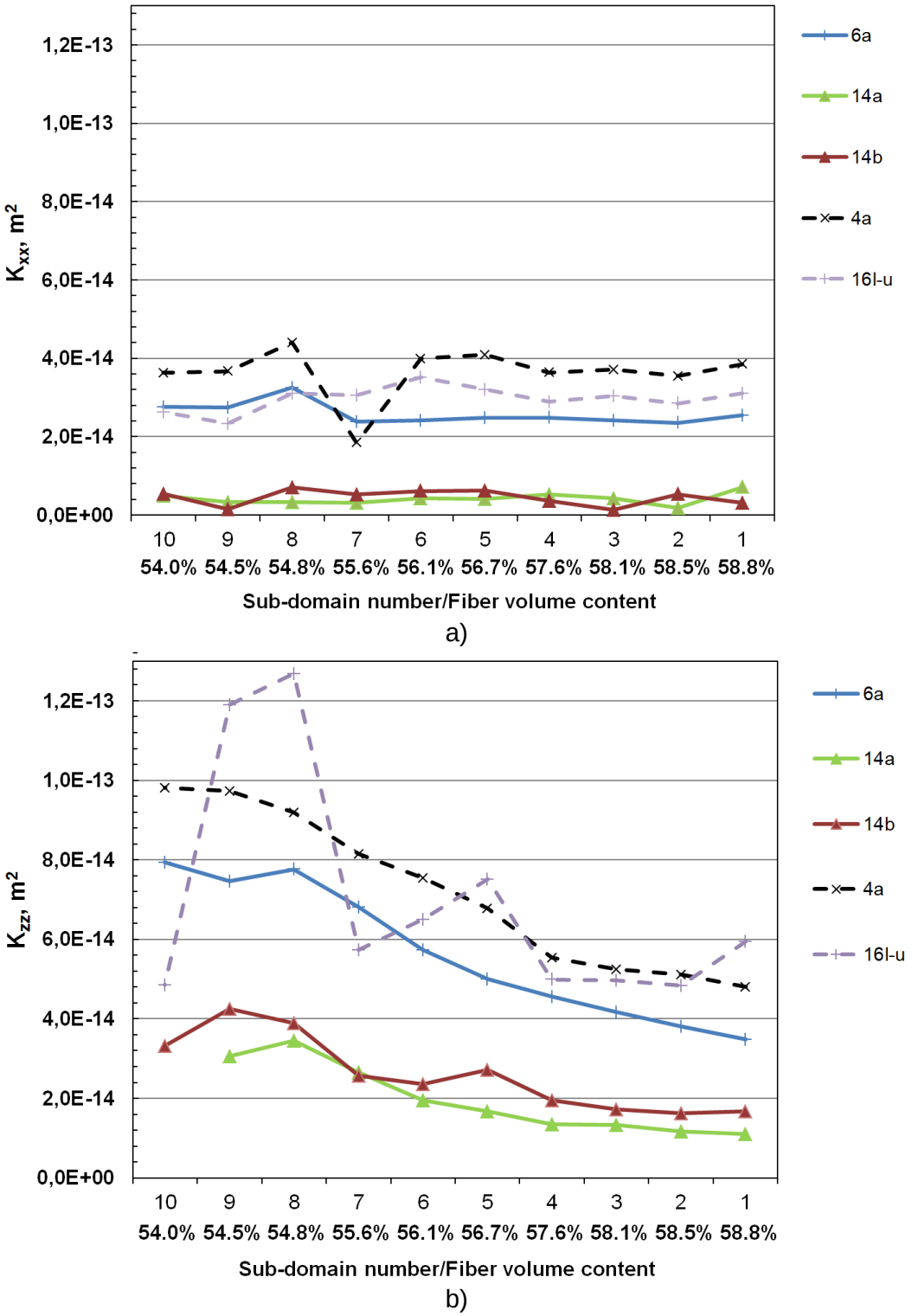

Figure 15: Evolution of the local permeability a) K_{xx}; b) K_{zz} computed on 10 sub-domains within the sample along the fiber direction (numbering of sub-domains corresponds to Fig. 9). 3D results are marked in dashed line

The observed lack of correlation between K_{xx} and FVC (Fig. 15a) may be due to the fact that all the tangential boundaries are very close to each other for the flow in the *Ox* direction (as opposed to the *Oz* direction) due to the dimensions of these 10 elongated subdomains (Fig. 9). Considering the trend of results #6b,c (their main tensor components almost coincide), despite their very high values mentioned above, both transverse permeability components K_{xx} and K_{zz} show an almost monotonic decrease with increasing FVC (Fig. 16).

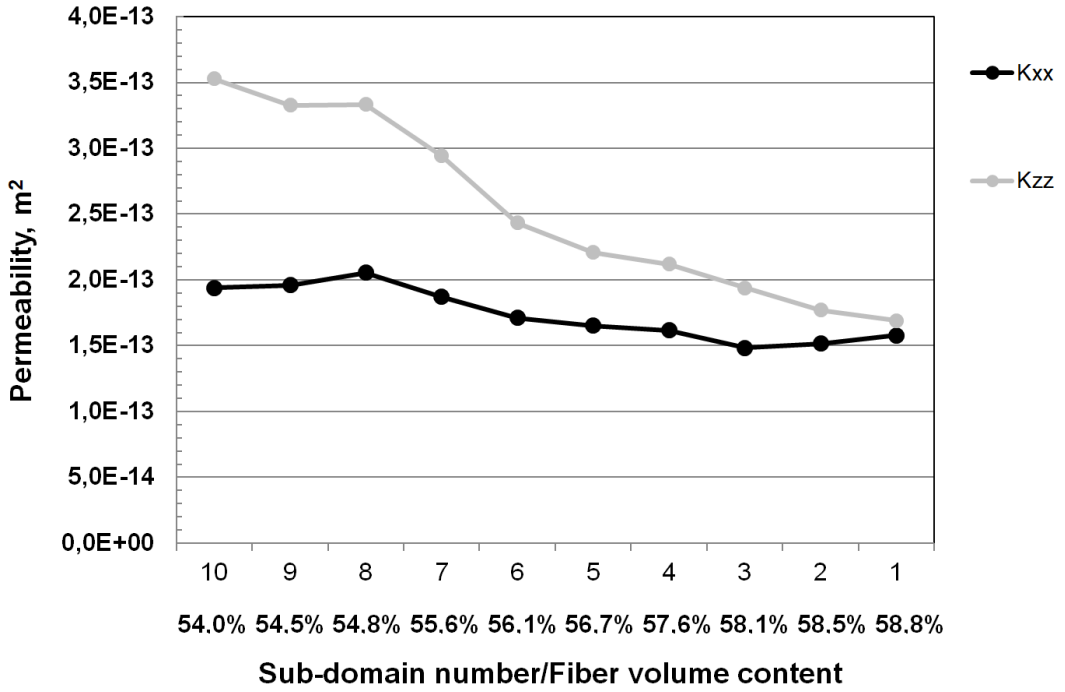

Figure 16: Evolution of the local permeability K_{xx} and K_{zz} computed for #6b,c on 10 slices uniformly distributed along the fiber direction

Unlike the results analyzed above, results #6b,c were calculated by averaging the computed fields with Darcy's law that takes into account transverse flows that can develop locally. All other results above (#4a, #6a, #14a,b) used the identification method with Darcy's law that does not allow one to calculate the full permeability tensor because it neglects the cross-flows. This can be a reason for these K_{xx} results to be less accurate.

4.3.2 3D computation results

Fig.17 shows the correlation between the transverse permeability (without the outliers identified above) and the fiber volume fraction. In contrast to the axial permeability, the reported transverse permeability values do not show the same decreasing trend with respect to increasing FVC, which was represented mainly by the #16l-u values calculated on the sub-volumes with evolving FVC along the fiber direction. These values are outlined in Fig.17a,b without a trend. However, as indicated in the previous section, the auxiliary values used for

the calculation of the result #4a and computed on the same 3D sub-volumes show a monotonic trend of K_{zz}, as shown in Fig. 17b.

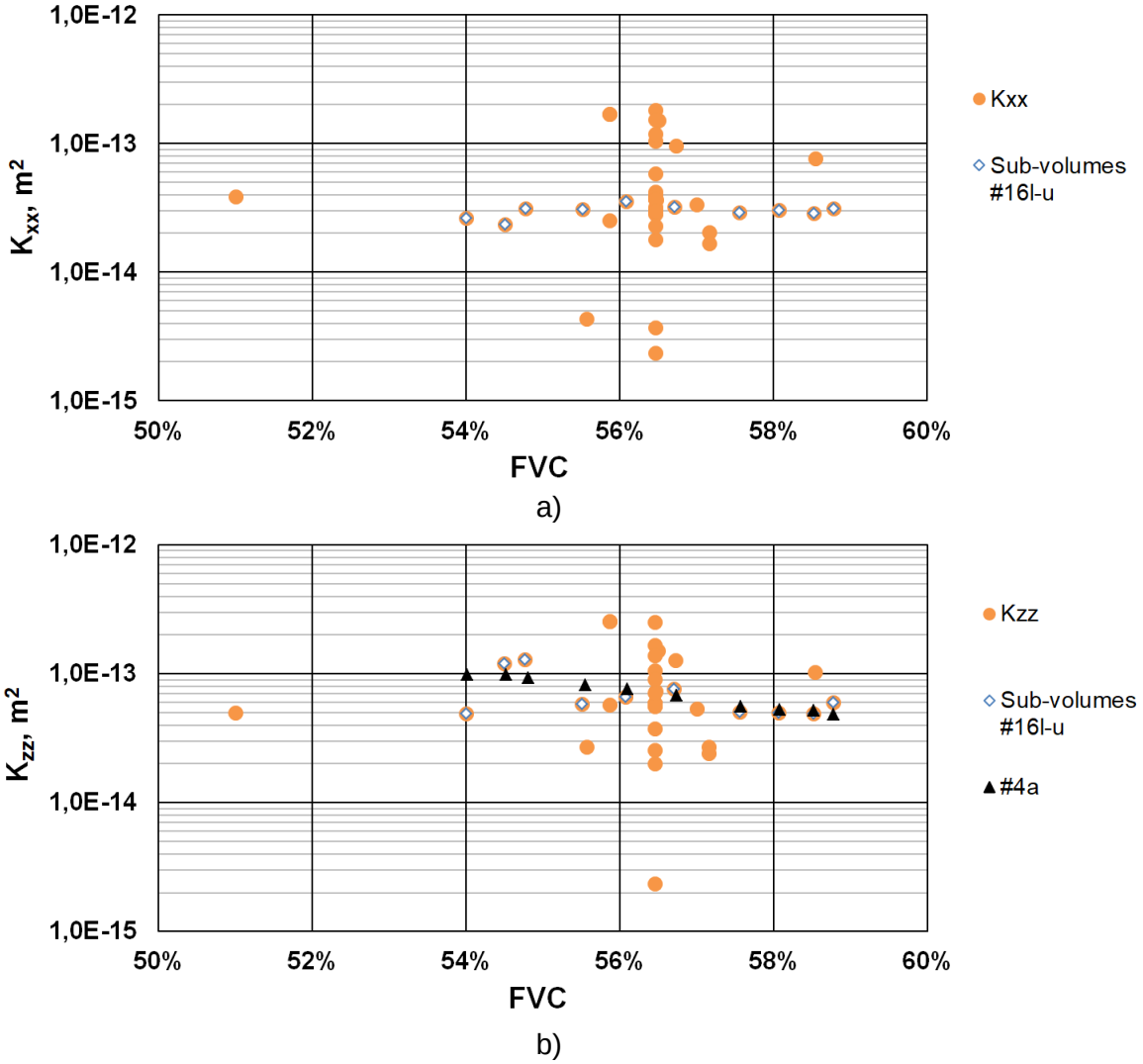

Figure 17: Correlation between the fiber volume fraction and predicted transverse permeability a) K_{xx}; b) K_{zz} (without excluded results #7a, #11, #13, #16b)

The components K_{xx} and K_{zz} are presented separately because they can be very different (Fig. 13): the cluster of values at FVC = 56.46% of the whole sample volume without the analytical values has a C_v of 85% for K_{xx}, while it equals 66% for K_{zz}.

The permeability values at 51% FVC correspond to the idealized microstructure of the result #15b. The lowest permeability values correspond to the analytical estimation of #4c. The values of participants #3 and #8a,b around 57% FVC characterize the whole 3D domain but with cropped edges.

Based on the analysis of the previous sections, it seems reasonable to consider the cluster of relevant transverse permeability values excluding the outliers mentioned above: the estimations based on idealized microstructures, the 2D results #2a,b, #6b,c, and #14a,b, the calculations on individual sub-volumes, as well as the results #16a-e,l-v using the

explicit-jump immersed interface method. The remaining results have a coefficient of variation of 24% for K_{xx} and 25% for K_{zz} with the mean values $\overline{K_{xx}}$ = 3,2E-14 m^2, $\overline{K_{zz}}$ =5,2E-14m^2.

4.3.3 Influence of cropping into sub-domains

A similar decreasing trend as for axial permeability is observed for the transverse permeability with increasing number of subdivisions of the domain, from which a permeability value of the whole domain is then deduced (Fig. 18). Similarly, results #16v and #8a do not follow this trend again. This can be explained by the fact that the result #8a was not obtained by the renormalization approach like the other results, as discussed earlier (see Section 4.2.1). Whereas result #16v was calculated from the #16l-u values on the sub-volumes cut transversely to the fiber direction (Fig. 9). However, as explained earlier, the explicit-jump immersed interface method apparently could not give adequate results in #16l-u, which were supposed to follow a decreasing trend with increasing FVC in the sub-volumes, but did not.

The minimal relative error with respect to the mean permeability value by replacing the volume by 10 sub-volumes is 15% for K_{xx} and 38% for K_{zz}. The maximal error corresponding to 648 sub-volumes is 48% for K_{xx} and 54% for K_{zz}.

Similarly to the findings on the axial permeability values, the study #3 about permeability convergence with increasing domain size showed that the whole sample domain should be used for computation because computations on smaller sub-domains did not provide stable permeability values.

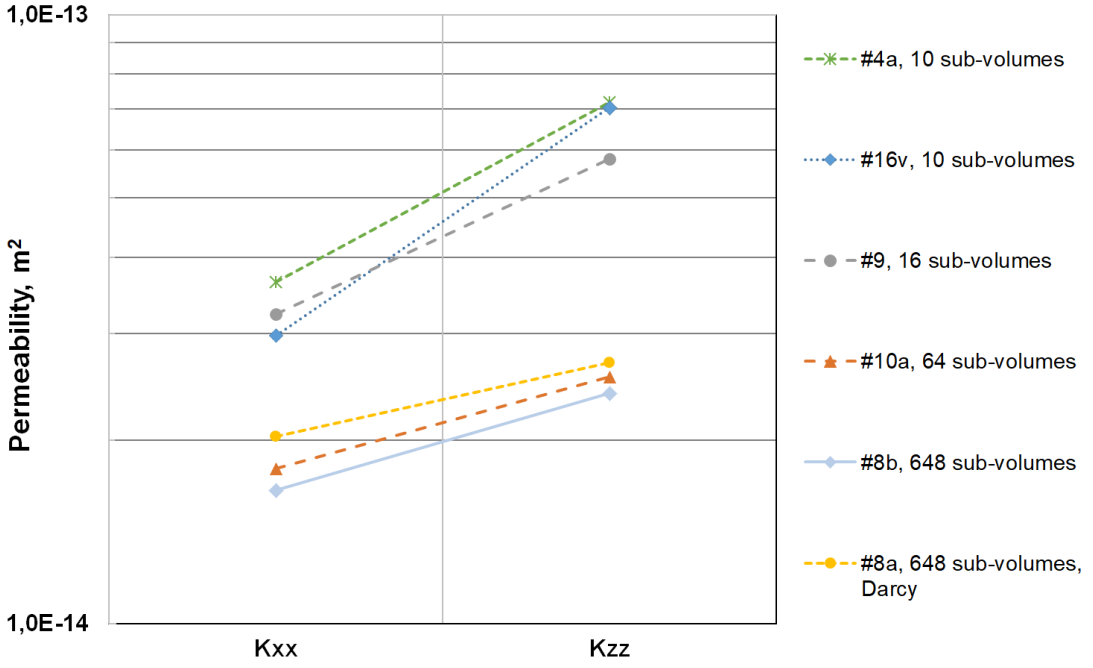

Figure 18: Transverse permeability K_{xx}, K_{zz} results #4a, #8a,b, #9, #10a, #16v computed by averaging the values from different number of sub-volumes

4.3.4 *Influence of boundary conditions*

In this section only the calculated or deduced (from sub-volumes) permeability values for the whole sample volume are considered. Similarly to the axial permeability analysis, first, we start by comparing the results obtained with the same methods and parameters, but with different BC (periodic/symmetric) (Fig. 19). One can see that the transverse permeability values K_{xx} computed with the symmetric BC are lower than those computed with the periodic BC, and thus show the opposite trend to the axial permeability (see Section 4.2.2).

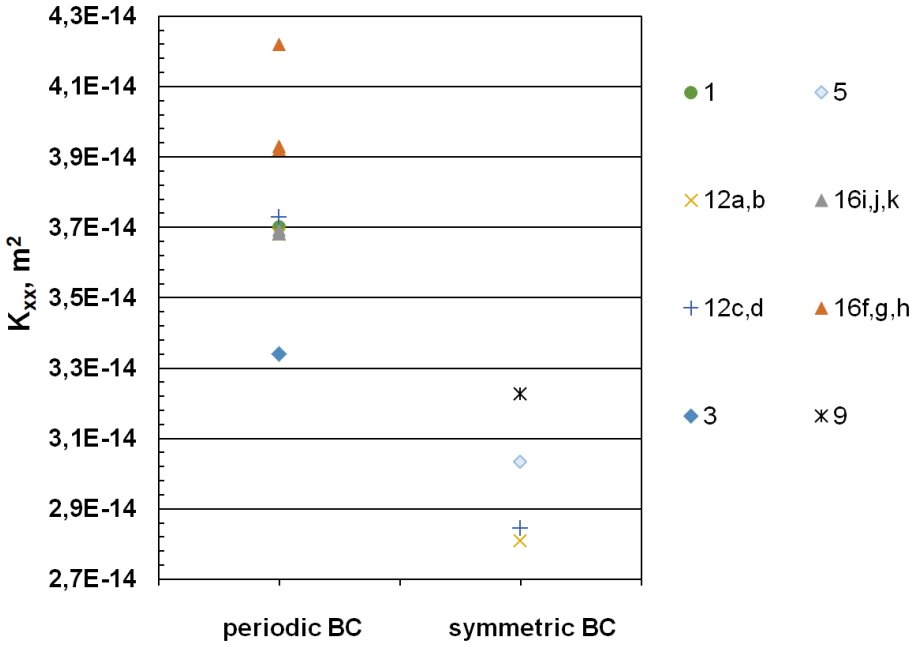

Figure 19: Transverse permeability K_{xx} values calculated in 3D by the same methods and different boundary conditions in tangential direction: periodic and symmetric

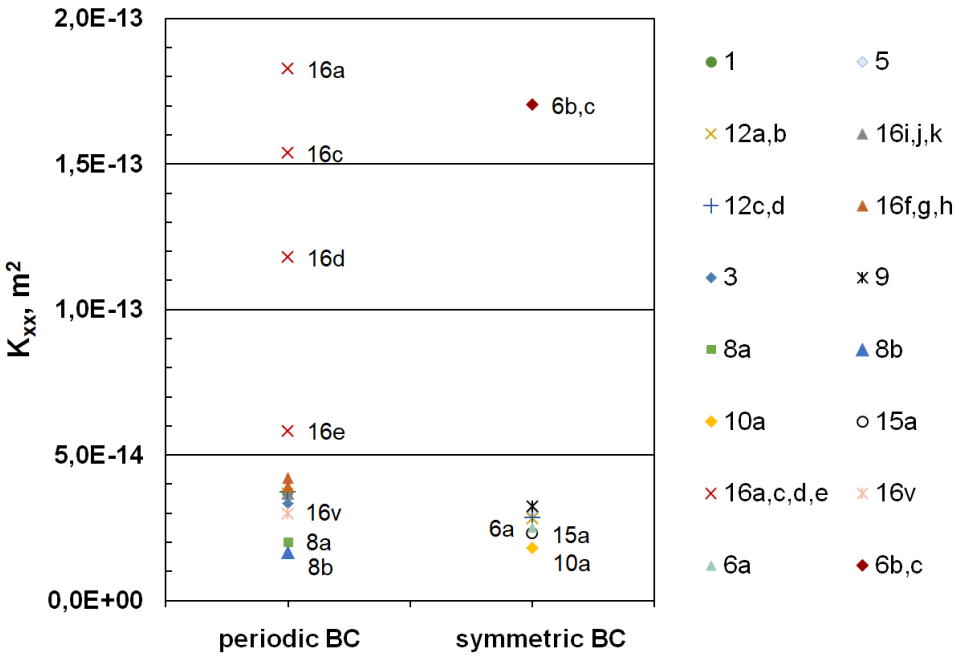

Figure 20: All transverse permeability K_{xx} values calculated/deduced for the whole sample volume with periodic and symmetric boundary conditions in tangential direction

If we add the rest of the results to this comparison (Fig. 20), including the 2D results #6a-c that also use the symmetric BC, the correlation shown above can no longer be observed.

For the transverse permeability component in the through-thickness direction K_{zz}, it is difficult to observe a clear trend even if one only compares results obtained by the same methods. Thus all results K_{zz} are plotted together in Fig. 21, and the ones obtained with different methods and parameters are marked in the graph with labels. Results #12a,b, as well as results #12c,d, which used exactly the same parameters and solver, are plotted with the lines to illustrate the slightly higher values obtained with periodic BC than with the symmetric ones, as for the transverse permeability K_{xx}. However, their relative difference is only 4%, while for K_{xx} it is 28% (for comparison: it was 9% for the axial permeability K_{yy}). Therefore, a very small influence of the imposed boundary conditions on the transverse permeability in the *Oz* direction can be observed.

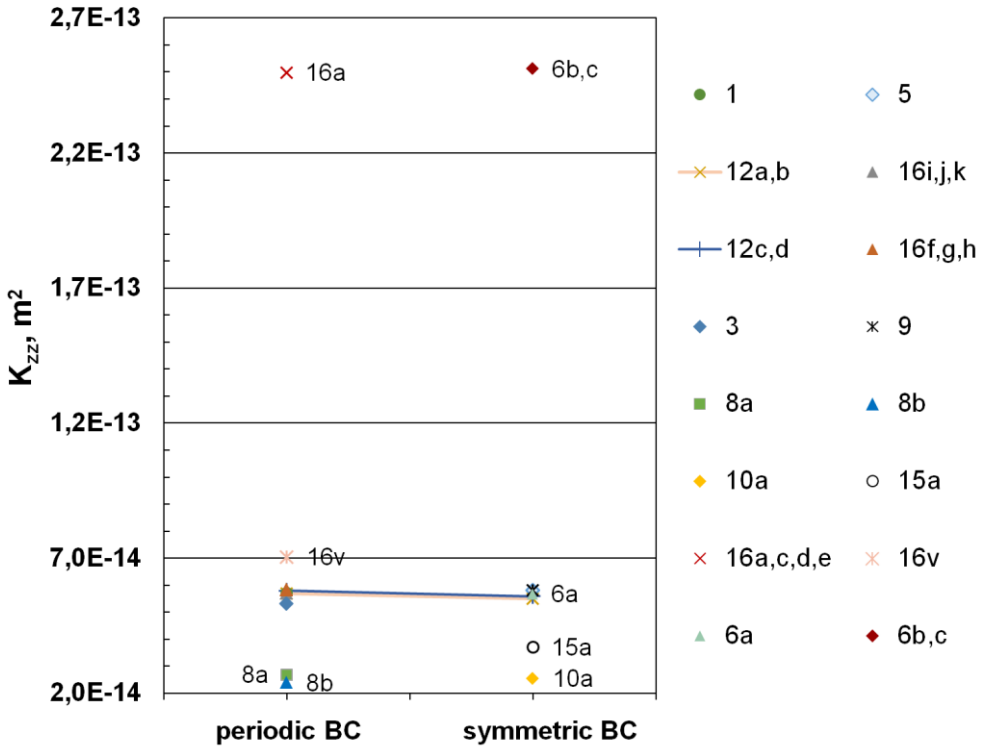

Figure 21: All transverse permeability K_{zz} values calculated/deduced for the whole sample volume with periodic and symmetric boundary conditions in tangential direction

It should be noted that the sample is a degenerated domain, commonly encountered in polymer composites, as the thickness is usually much smaller than the in-plane dimensions due to the compaction of layered structures. Consequently, the flow across the thickness (direction *Oz)* is barely influenced by the lateral boundaries. On the contrary, the flows in *Ox* and *Oy* directions are strongly influenced in this case by one pair of tangential flow boundaries (in the *Oxy* plane) situated close to each other. Moreover, for the transverse

permeability K_{xx} periodic BC give higher values of permeability than the symmetric ones, while for the axial permeability K_{yy} periodic BC give lower values.

Similarly to the axial permeability K_{yy}, the K_{xx} and K_{zz} results of participants #12a and #16i,j,k, using exactly the same conditions and method, have an excellent agreement (for a given solution precision).

Similarly to the axial permeability, there is no apparent trend in the transverse permeability values with increasing length of the inflow / outflow regions when the results using the same methods and conditions are analyzed together: #1 and #12a, #5 and #12d (Fig. 3, 4 in the Supplementary material).

4.4 Influence of flow model

Six out of 16 participants used the Navier-Stokes equations instead of Stokes (Table 2). In the previous sections, some of them have been eliminated from the analysis as outliers, so they are omitted below.

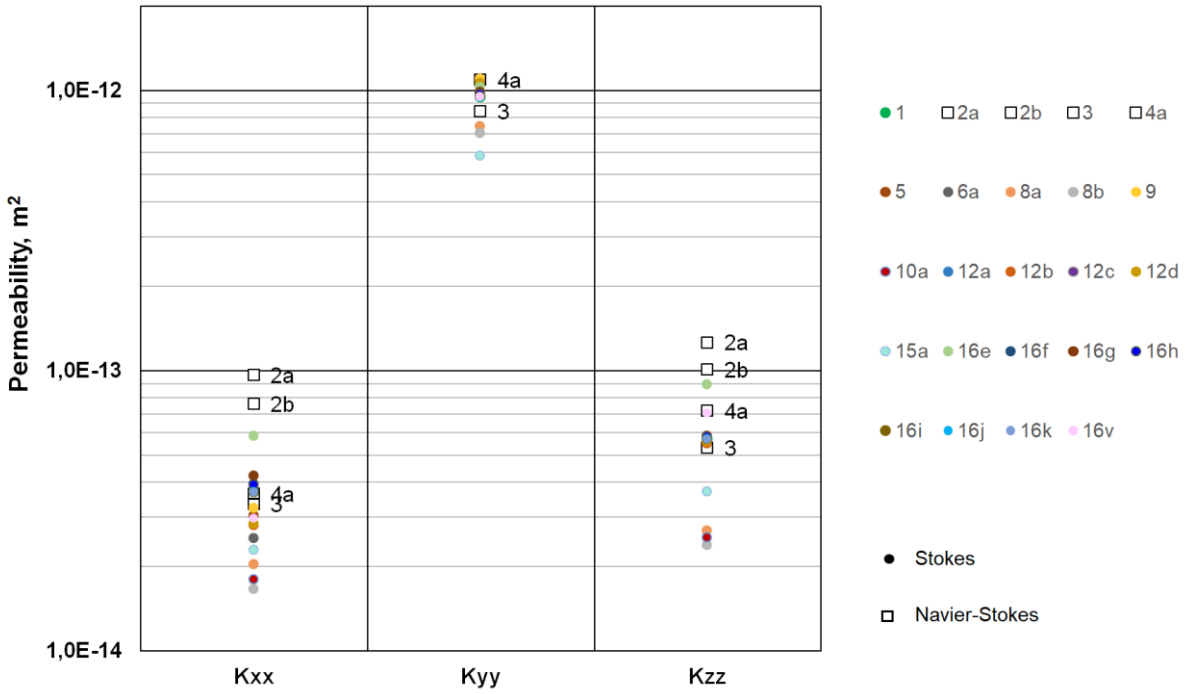

Figure 22: Permeability values obtained by the Navier-Stokes model (labeled in the graph) and Stokes equation (without excluded results #7a, #11, #13, #16a-d, #6b,c, #14a,b, and #15b as computed on the idealized structure, as well as #10b,#16l-u as computed on sub-volumes only)

Fig. 22 shows the scatter of the results that used Navier-Stokes equations, without any particular correlation to the results obtained by solving the Stokes equation. In case of Navier-Stokes flow simulations a very small local Reynolds number of the flow through the pores was ensured by the participants: #2 reported the Reynolds number estimations between 1E-4 and 1E-3; #3 in the order of ~1E-4; #4 estimated it in the order of ~1E-8 for the

transverse to fibers flow and ~1E-7 for the axial flow. All in all, no particular influence of the flow model was found.

4.5 Analysis of the full permeability tensor

Three different approaches were used by the participants to calculate the permeability values from the velocity/pressure fields: i) identification with Darcy's law using the averaged flow rate without considering cross-flows; ii) identification with Darcy's law, based on the volume averaging principles that take into account transverse flows [28]; iii) full-field homogenization [29]. Approach ii) averages the computed velocity/pressure fields, which in the case of anisotropic structure contain the information about the developed cross-flows, and thus allows to reconstruct the full permeability tensor. Homogenization methods are generally those that use a localization tensor to relate fields at different scales. Localization tensors can be constructed either by the mean-field approaches based on the Eshelby tensor for dilute configuration [30], or the Mori-Tanaka scheme for higher concentration [31,32]; or by the direct numerical solution of the full-field problem without approximating the geometry and distribution of the constituent phases [29] (full-field homogenization).

The results on the full permeability tensor can be found in the Supplementary material. The use of the identification procedure without considering the cross-flows implies that the flow is necessarily forced in principal directions, and only the supposed non-zero diagonal terms of the permeability tensor can then be calculated. However, the order of magnitude of the off-diagonal/skew terms obtained by the participants who applied the approaches ii) and iii), reaching in some cases ~1E-14 m^2, shows that these terms are not negligible. This can be attributed to the twisted structure of the tow with 40 twist/m, i.e. one complete twist each 25 mm, which is much bigger than the tow length of the MSV. The diagonalization of the permeability matrix of e.g., #15a indicates that the structure has a rotation of approximately 17° in the *Oxz* plane, which is perpendicular to the fiber direction.

Two participants #2 and #6b,c computed the full permeability tensor in 2D. However, these results show rather high values of the principal tensor components compared to the identified cluster of results.

It should also be noted that the permeability tensor computed by some participants was non-symmetric. It was obtained by an approach where, after forcing the flow in three independent directions (two in 2D), each of the solutions provided independently a column of components of the permeability tensor at a time, without ensuring their symmetry. However, the symmetry of the permeability tensor should be respected, as shown, for example, in [33-34].

4.6 Results based on idealized microstructure

Some participants also studied the possibility to estimate the permeability of the sample fiber bundle by some known analytical models [25-27], or on a virtually generated fiber bundle, which aimed at reproducing the main features of the sample. These analyses are detailed in the Supplementary material. It is shown that Gebart's analytical models with their assumptions rather give a lower bound for the axial permeability of this unidirectional microstructure than a good estimation of its cluster mean, and an upper bound for the transverse permeability. As far as a virtually generated microstructure is concerned, at this stage it cannot be concluded whether it can adequately replace the real microstructure.

5 Conclusions

The objective of this first virtual permeability benchmark exercise was, firstly, to provide a state-of-the-art of existing numerical approaches for permeability prediction based on real fibrous microstructures, and, secondly, to gain insights into the dominant parameters influencing its determination.

Although the first stage of the benchmark was devoted to the micro-scale permeability of a fiber tow, i.e. a relatively simple transversely isotropic structure, and although the image processing effect was eliminated by the use of the segmented microstructure image provided to all participants, the coefficient of variation of the reported results was large. However, the analysis of the reported values with respect to different parameters showed that the cluster of the most relevant results has a reduced coefficient of variation C_v of 14% for the axial permeability K_{yy}, and 24% and 25% for the components K_{xx} and K_{zz} of the transverse permeability, respectively (Table 4). It is most likely due to the less complex geometry of the sample microstructure in the axial direction, implying less complex flow paths, that it gave rise to a lower scatter of the axial permeability than that of the transverse permeability. The same trend was observed when the influence of different parameters was analyzed: cropping into sub-domains, boundary conditions, etc.

Table 4: Data on the resulting cluster of permeability values

	K_{xx}	K_{yy}	K_{zz}
mean $\overline{K}$	3,2E-14 m^2	9,4E-13 m^2	5,2E-14 m^2
C_v	24%	14%	25%

For this case, higher values of the transverse permeability K_{zz} were obtained than K_{xx} because the domain in the through-thickness sample direction was ⅛ of the in-plane

direction. The results computed on smaller sub-volumes showed that taken solely each of them could not be representative of the whole sample. Besides, the influence of applied boundary conditions becomes negligible as the domain becomes larger. This was observed for the case of K_{zz} component by applying different BC in the tangential direction. In general, the effect of the BC applied in the tangential direction was found to be dominant with respect to the effect of BC applied in the flow direction. Systematically, the axial permeability values calculated with symmetric BC were higher than those calculated with periodic BC, while this trend was the opposite for the transverse permeability K_{xx}. It should be noted that the no-slip and symmetric BC are not convenient particularly when the permeability tensor is expected to have non-zero off-diagonal terms because these BC prevent the development of transverse flows.

In addition to boundary conditions in tangential direction, a crucial influence on permeability prediction is exerted by the 2D or 3D formulation of the problem. No conclusion can be drawn on the possibility of substituting the given 3D microstructure by a set of 2D sub-domains. Some 2D results underestimated the permeability, while some of them overestimated it. The result that used all 2D cross-sections of the sample and calculated the permeability by the identification with Darcy's law without considering the cross-flows gave values which were within the main cluster. However, this solution did not have a correct dependency on the fiber volume fraction, which was the case for the result calculated on the same flow fields but with Darcy's law taking into account transverse flows. This confirms once again the necessity to use approaches capable of calculating the full permeability tensor.

Another important source of variation in permeability results is the number of sub-volumes used to calculate, first, local permeabilities and then the global permeability. The higher the number of cropped sub-volumes, i.e. the higher the number of artificial boundaries introduced into the domain, the lower the predicted permeability is. Calculating the permeability of the entire sample by this renormalization approach can be a good solution if the number of sub-volumes is not too high and in cases where the computational resources are limited in terms of memory or time. The minimal number of sub-volumes (10) used in the benchmark study resulted in only 15% deviation from the cluster average value. It should be noted, however, that the agreement of results obtained by this approach is highly dependent on the fibrous architecture and, particularly, on the presence of anisotropy effects.

The influence of other factors, such as physical variables formulation, flow model, numerical method, discretization, on the permeability was either dominated by the above mentioned parameters, or did not reveal any trends and dependencies in the permeability.

The key points for permeability determination can be summarized as follows. To address the creeping flow condition in prediction of permeability of porous medium, the Stokes

equation should be used. For microstructures with unknown principal directions or with anisotropic effects, the application of symmetric or no-slip boundary conditions is not appropriate. For permeability identification, it is important to use a method that allows to calculate the full permeability tensor, which is a symmetric and positive definite second order tensor.

It is planned to use the average values of the cluster of computed permeability values of tows of the used twill-weave fabric as an input for meso-scale calculations of flow through the fabric to deduce its macroscopic permeability, to which the next stage of the benchmark will be dedicated.

6 Acknowledgments

M. Matveev and A. Endruweit are grateful for the support through the University of Nottingham's Digital Initiatives programme and access to the Augusta HPC service. M. Matveev was supported by the Engineering and Physical Sciences Research Council, UK, through the EPSRC Future Composites Manufacturing Research Hub [EP/P006701/1].

7 Declaration of conflicting interests

The author(s) declare no potential conflicts of interest with respect to the research, authorship, and/or publication of this article.

References

[1] Simacek P., Advani S.G. (2004) Desirable Features in Mold Filling Simulations for Liquid Composite Molding Processes. Polymer Composites 25 (4): 355-367.
[2] ESI-Group. PAM-RTM Simulation Software of the Resin Transfer Molding (RTM) Process. https://www.esi-group.com/
[3] Koorevaar A. (2002) Simulation of Liquid Injection Moulding. Proceedings of the 23rd International SAMPE Europe Conference, Paris, France – 2002: 633-644.
[4] Wang J., Simacek P., Gupta N., Advani S.G. (2018) Multidisciplinary tool for composite wind blade design & analysis. Composites Part B: Engineering 140: 91-98.
[5] Darcy H. (1856) Les Fontaines Publiques de la ville de Dijon, Paris: Libraire des Corps Impériaux des Ponts et Chausses et des Mines.
[6] Yong, A.X.H., Aktas, A., May, D., et al. (2021) Out-of-plane permeability measurement for reinforcement textiles: A benchmark exercise. Composites Part A: Applied Science and Manufacturing 148: 106480.
[7] May D., Aktas A., Advani S. G., et al. (2019) In-plane permeability characterization of engineering textiles based on radial flow experiments: A benchmark exercise. Composites Part A: Applied Science and Manufacturing 121: 100-114.

[8] Becker D., Grössing H., Konstantopoulos S., et al. (2016) An evaluation of the reproducibility of ultrasonic sensor-based out-of-plane permeability measurements: a benchmarking study. Advanced Manufacturing: Polymer & Composites Science 2 (1): 34-45.
[9] Grössing H., Becker D., Kaufmann S., et al. (2015) An evaluation of the reproducibility of capacitive sensor based in-plane permeability measurements: A benchmarking study. Express Polym. Lett. 9 (2): 129-142.
[10] Vernet N., Ruiz E., Advani S., et al. (2014) Experimental determination of the permeability of engineering textiles: Benchmark II. Composites Part A: Applied Science and Manufacturing 61: 172-184.
[11] Arbter R., Beraud J.M., Binetruy C., et al. (2011) Experimental determination of the permeability of textiles: A benchmark exercise. Composites Part A: Applied Science and Manufacturing 42: 1157-1168.
[12] Zarandi M.A.F., Arroyo S., Pillai K.M. (2019) Longitudinal and transverse flows in fiber tows: Evaluation of theoretical permeability models through numerical predictions and experimental measurements. Composites Part A: Applied Science and Manufacturing 119: 73-87.
[13] Hwang W.R., Advani S.G. (2010) Numerical simulations of Stokes-Brinkman equations for permeability prediction of dual scale fibrous porous media. Physics of Fluids 22 (11): 113101.
[14] Syerko E., Binetruy C., Comas-Cardona S., Leygue A. (2017) A numerical approach to design dual-scale porosity composite reinforcements with enhanced permeability. Materials and Design 131: 307-322.
[15] Straumit I., Hahn C., Winterstein E., et al. (2016) Computation of permeability of a non-crimp carbon textile reinforcement based on X-ray computed tomography images. Composites Part A: Applied Science and Manufacturing 81: 289-295.
[16] Geoffre A., Ghestin M., Moulin N., et al. (2021) Bounding transverse permeability of fibrous media: a statistical study from random representative volume elements with consideration of fluid slip. International Journal of Multiphase Flow 143: 103751.
[17] Zeng X., Brown L.P., Endruweit A., et al. (2014) Geometrical modelling of 3D woven reinforcements for polymer composites: Prediction of fabric permeability and composite mechanical properties. Composites Part A: Applied Science and Manufacturing 56: 150-160.
[18] Raizada A., Pillai K.M., Ghosh P. (2022) A validation of Whitaker's closure formulation based method for estimating flow permeability in anisotropic porous media. Composites Part A: Applied Science and Manufacturing 156: 106831.
[19] Salvatori D., Caglar B., Teixidó H., Michaud V. (2018) Permeability and capillary effects in a channel-wise non-crimp fabric. Composites Part A: Applied Science and Manufacturing 108:41-52.
[20] Shakoor M., Park C.H. (2022) Computational homogenization of unsteady flows with obstacles. International Journal for Numerical Methods in Fluids: 1-29.
[21] Abouorm L., Troian R., Drapier S., et al. (2014) Stokes-Darcy coupling in severe regimes using multiscale stabilisation for mixed finite elements: monolithic approach versus decoupled approach. European Journal of Computational Mechanics 23 (3-4): 113-137.
[22] Wiegmann A., Bube K.P. (2000) The explicit-jump immersed interface method: finite difference methods for PDEs with piecewise smooth solutions. SIAM Journal on Numerical Analysis 37 (3): 827-862.
[23] Linden S., Wiegmann A., Hagen H. (2015) The LIR space partitioning system applied to the Stokes equations. Graphical Models 82: 58-66.
[24] Guibert R., Horgue P., Debenest G., Quintard M. (2016) A comparison of various methods for the numerical evaluation of porous media permeability tensors from pore-scale geometry. Mathematical Geosciences 48 (3): 329-347.
[25] Gebart B.R. (1992) Permeability of Unidirectional Reinforcements for RTM. Journal of Composite Materials 26 (8): 1100-1133.
[26] Endruweit A., Gommer F., Long A.C. (2013) Stochastic analysis of fibre volume fraction and permeability in fibre bundles with random filament arrangement. Composites Part A: Applied Science and Manufacturing 49: 109-118.

[27] Tamayol A., Bahrami M. (2009) Analytical determination of viscous permeability of fibrous porous media. International Journal of Heat and Mass Transfer 52 (9-10): 2407-2414.
[28] Gray W.G., Miller C.T. (2013) A generalization of averaging theorems for porous medium analysis. Advances in Water Resources 62: 227-237.
[29] Lopez E., Abisset-Chavanne E., Lebel F., et al. (2016) Flow modeling of linear and nonlinear fluids in two and three scale fibrous fabrics. International Journal of Material Forming 9 (2): 215-227.
[30] Eshelby J.D. (1957) The determination of the elastic field of an ellipsoidal inclusion, and related problems. Proceedings of the Royal Society London A 241: 376-396.
[31] Dormieux L., Kondo D., Ulm F.J. (2006) Microporomechanics. John Wiley & Sons Inc.
[32] Tran T., Comas-Cardona S., Abriak N.-E., Binetruy C. (2010) Unified microporomechanical approach for mechanical behavior and permeability of misaligned unidirectional fiber reinforcement. Composites Science and Technology 70 (9): 1410-1418.
[33] Neuman S.P. (1977) Theoretical Derivation of Darcy's Law. Acta Mechanica 25: 153-170.
[34] Atherton T.J, Kerbyson D.J. (1999) Size invariant circle detection. Image and Vision Computing. 17 (11): 795-803.
[35] Cai Z., Berdichevsky A.L. (1993) Numerical simulation on the permeability variations of a fiber assembly. Polymer Composites 14 (6): 529-539.
[36] Chen X., Papathanasiou T.D. (2007) Micro-scale modeling of axial flow through unidirectional disordered fiber arrays. Composites Science and Technology 67 (7-8): 1286-1293.
[37] Lundström T.S., Gebart B.R. (1995) Effect of perturbation of fiber architecture on permeability inside fiber tows. Journal of Composite Materials 29 (4): 424-443.
[38] Chen X., Papathanasiou T.D. (2008) The transverse permeability of disordered fiber arrays: a statistical correlation in terms of the mean nearest inter fiber spacing. Transport in Porous Media 71 (2): 233-251.
[39] Chen L., Gu B., Zhou J. (2019) Development of the RSA method for random short fiber reinforced elastomer composites with large fiber aspect ratios. Materials Research Express, IOP Publishing 6 (6): 065322.
[40] Ge W., Wang L., Sun Y., Liu X. (2019) An efficient method to generate random distribution of fibers in continuous fiber reinforced composites. Polymer Composites 40 (12): 4763-4770.

Supplementary material

1 Materials & Data Preparation

1.1 Materials & Manufacturing of the composite sample

In order to provide a real microstructure for the virtual permeability benchmark calculations, a composite plate was manufactured with the resin transfer molding process, and a sample was cut out of the plate and scanned with an X-ray microscope. To manufacture the sample plate, 14 layers of the glass fiber fabric Hexcel HexForce 01102 1000 TF970 were placed at the same orientation in an isochoric cavity with the size of 465 x 465 mm^2 and a height of 3.0 mm. The same fabric was used in the experimental permeability benchmark exercise [7]. The fiber reinforcement was then impregnated using the epoxy resin system (EP) Hexion EPIKOTE^{TM} Resin MGS^{TM} RIMR 935 with EPIKURE^{TM} Curing Agent MGS^{TM} RIMH 936 in a mixing ratio of 100 : 29 in parts by weight. The resin-hardener mixture was degassed in a vacuum vessel for about 5 minutes at below 100 Pa before injection. Furthermore, a vacuum was also created in the mold cavity before injection for the reason of checking the tightness of the mold and reducing voids formation in the composite. The resin injection took place at a mold temperature of 80°C and a pressure of 6 bars. To cure the EP, the temperature was kept at 80°C for further 3.5 hours. This configuration resulted in a 54% fiber volume content (FVC) within the plate. Thus, a FVC of more than 54% is expected within the microstructure extracted from a fiber bundle within this textile composite.

Glass fiber fabric

The glass fiber fabric Hexcel HexForce 01102 1000 TF970 is a balanced twill weave 2/2 (weight distribution: 50% warp / 50% weft) with a nominal weight of 295 g/m^2. The thread count of the twill weave is 7 tows/cm each in warp and weft direction. The fiber bundles in the textile consist of three EC9 68 tex glass fiber yarns twisted in a tow (40 twist/m). According to the nomenclature, these are continuous filaments of E-glass with a nominal diameter of 9 µm. The variation of fiber diameters was checked with the help of 6 micrographs. For each micrograph at least 50 fibers from 3 different tows were measured. Thus, a total number of more than 900 fiber diameters were measured by manually reproducing the fiber circumference using three points on it. The average fiber diameter was found to be 9.3 µm with a standard deviation of 0.35 µm.

1.2 Imaging & Segmentation

In order to ensure a sufficiently high quality of the images of the microstructure to distinguish single fibers, the resolution and the contrast between the materials – glass and epoxy resin – must be as high as possible. To achieve this, the sample for the scan should be approximately the same size as the region of interest (ROI). Therefore, a cut-out of the plate of 1 x 1 x 3 mm^3 was prepared with a precision cutter under permanent cooling. The cooling in combination with a slow cutting speed reduces the heat input into the specimen and thus minimizes the influence on the specimen. The 3D scan of the specimen was performed using the Zeiss Xradia 520 Versa 3D X-ray Microscope at IVW. The scan has a volume of approximately 1 mm^3. This corresponds to 2000^3 voxels with the size of 0.521^3 μm^3. With the objective to determine the permeability of the microscale fiber structure, a sub-volume of the scan was extracted within a fiber bundle covering all bundle height and containing about 400 fibers in width and over a length of 507 µm. This sub-volume had a size of 1003x124x973 voxels (523 x 65 x 507 μm^3) and represented the microscale volume (MSV) for the study in the benchmark. The diameters of fibers of the MSV varied within the range 7.5 - 9.3 µm, and the average over the MSV fiber volume fraction was 56.46% (Table 1).

Table 1: Microstructural parameters of the considered microscale volume (MSV)

Fibers diameter	Fiber volume fraction	Dimensions of the MSV
8,4 ± 0,9 µm	56,46 %	523 x 65 x 507 μm^3

During the scan, each voxel is assigned a gray value proportional to the absorption of X-rays by the respective body volume. Since the materials glass and epoxy resin absorb the X-rays differently, the voxels representing glass fibers have a different gray value than voxels representing epoxy resin. However, various influences or process-related factors can cause different image artifacts and affect the gray values. The fact that there is no exact separation at the material transition, but rather an undefined transition also complicates the image processing, namely the segmentation intending to “separate” fibers from the matrix. The segmentation generates content-related regions by combining neighboring voxels according to a certain homogeneity criterion, such as a defined gray value range, for example.

The afore-mentioned features of the tows, such as fibers twisting and misalignment, different fibers diameters, but also a limited voxel size made the volume segmentation procedure non-trivial. Indeed, conventional gray-level thresholding resulted in the presence of unrealistic inter-fiber "bridges" that could have a significant impact on subsequent permeability predictions. Therefore, a more complex image processing procedure was adopted to segment fibers from the inter-fiber porous space/matrix. It consisted in the following steps (Fig. 1). Since the fibers of this fabric have a circular cross-section shape, it

was convenient to treat the 3D volume slice by slice by applying the circular Hough transform [34] in order to detect the cross-sections centers and estimate their size within the radii range. Due to fiber misalignment, the 3D structure of the tow cannot be considered as an extrusion of a 2D slice transverse to the fiber direction. Hence, this step was conducted on each 2D slice separately. Then the detected fibers were labeled and their paths across the stack of 2D slices were identified using the nearest neighbor algorithm. Finally, due to the previously applied 2D processing, a smoothing of the 3D fiber paths through the volume was performed by local regression using weighted linear least squares and a 1st degree polynomial model. As a result, a segmented binary volume with two phases – fibers and pores – was obtained.

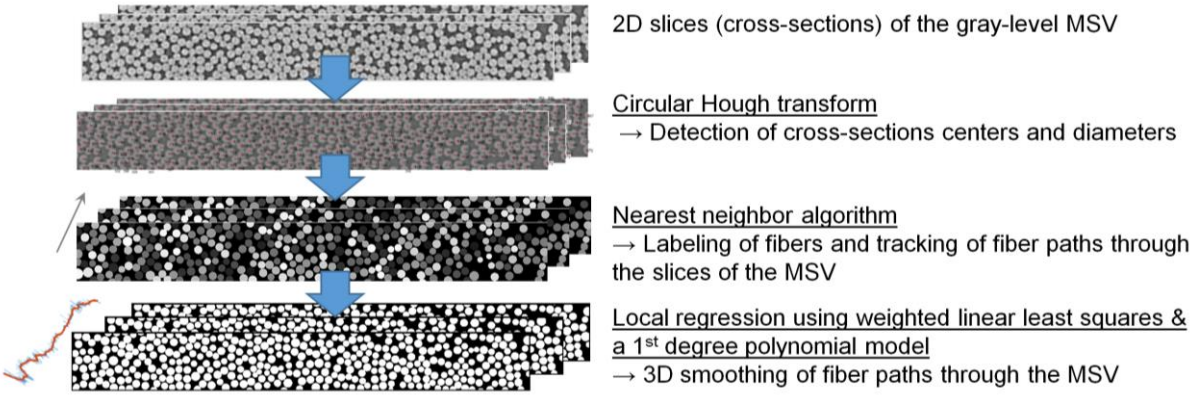

Figure 1: Segmentation procedure for the microscale volume (MSV)

1.3 Data Set & Task Definition

The data package for the first stage of the VPB consisted of the guidelines with a detailed questionnaire and two different data sets of the sample microstructure: a file with the segmented 3D volume and a corresponding stack of segmented 2D images, as well as a non-segmented 3D volume file and a corresponding stack of non-segmented 2D images. The 3D and corresponding 2D data can be found on the repository at https://doi.org/10.5281/zenodo.6611926. The participants of the benchmark had a mandatory task to fill out the questionnaire describing the steps and methods of their computational procedure, and to compute the permeability tensor based on the segmented MSV. Since the sample segmentation procedure can have a significant impact on the resulting microstructure representation in the image and thus the permeability, participants were provided with the segmented data to eliminate this source of variation. Apart from this, no restrictions were imposed at this first stage of the virtual permeability benchmark. For example, the participants could reduce the volume, split it into the sub-volumes, or make calculations only on a set of 2D slices.

As an optional task, participants could use the provided non-segmented data to perform the segmentation and then determine the permeability tensor. Another option was to analytically estimate the permeability of the provided microstructure.

2 Technical characteristics of computations

In Table 2 the technical characteristics of the used computational resources and simulation times for all results of the benchmark are summarized. It can be observed that the methods were implemented on computers with very different performance, were parallelized in different ways, and different discretization resulted in a different number of degrees of freedom (DOFs). Therefore, the simulation times can hardly be compared, even being normalized by the number of DOFs.

Table 2: Computational resources and simulation times

Result #	CPU-GPU characteristics of given computing nodes	Memory used, Gb	Number of used parallel processes	Run time, hours
1	Intel® Xeon® CPU E5-2660 @ 2.20GHz	17	16	1,5
2	Intel® Xeon® CPU W-2175 @ 2.50GHz	20	1	6 for 10 2D slices
3	Intel® Xeon® Gold CPU 6138 @ 2.0GHz, 20 Core(s)	88	10	28,8
4	Intel® Xeon® CPU E5-2667 v3 @ 3.20GHz,16 Core(s), 16 Logical Processor(s)	60-70	12 or 16	Kxx: 1-1,5 Kyy: 1,5-2 Kzz: 1
5	Intel® Core™ i7-8700K CPU @ 3.70GHz	8,9	11	Kxx: 3,8 Kyy: 0,1 Kzz: 0,1
6	Intel® Core™ i7-8650U CPU @ 1.90GHz	10	4	136,2 for 973 2D slices
7	Intel® Xeon® CPU E5-2650 v2 @ 2.60GHz, 16 Core(s)	9,7	1	5,9
8	Intel® Core™ i5-8350U CPU @ 1.70GHz 1.90GHz	2	1	18
9	Intel® Xeon® CPU E5-2630B4 @ 2.20GHz	50	4	16
10	Intel® Xeon® (Haswell) CPU E5-2860 v3 @ 2.50GHz	15	2	35
11	Intel® Core™ i5-6500TE CPU @ 2.30GHz	22	4	5,8
12a	Intel® Xeon® CPU E5-2680 @ 2.80 GHz Dual Core	9,1-10,4	8	6,6
12b	- ·· -	9,1-10,4	- ·· -	7,3
12c	- ·· -	2,9-3,0	- ·· -	18,4
12d	- ·· -	2,8-3,0	- ·· -	26,6
13	Intel® Xeon® CPU E5-2637 v4 @ 3.50GHz, 2 Logical Processor(s)	10,0	2	16,4
14	AMD Ryzen 7 2700 @ 3.20GHz, 8 Core(s), 16 Logical Processor(s)	8	1	24
15	Intel® Xeon® (Haswell) CPU E5-2860 v3 @ 2.50GHz	180	288	1,5
16	Intel® Xeon® CPU E5-2630 v22 @ 2.60GHz, 6 Core(s)	12,7-13,4	4	6,2

3 Influence of boundary conditions in flow direction

Participants #1, #5, #10, #12, and #16 additionally used both the inflow and outflow regions of equal length. All other parameters and conditions in #5 and #12d were the same, except for this length: 40 voxels and 10 voxels per region respectively. Another pair of results #1 and #12a also differ from each other only by the inflow / outflow regions length: 96 and 10 voxels, respectively. The analysis of these values (Fig. 2, 3, 4) shows that there is no apparent trend in permeability values with increasing length of these channels, or that their effect is dominated by other more influencing factors, such as the BC in tangential direction, for instance.

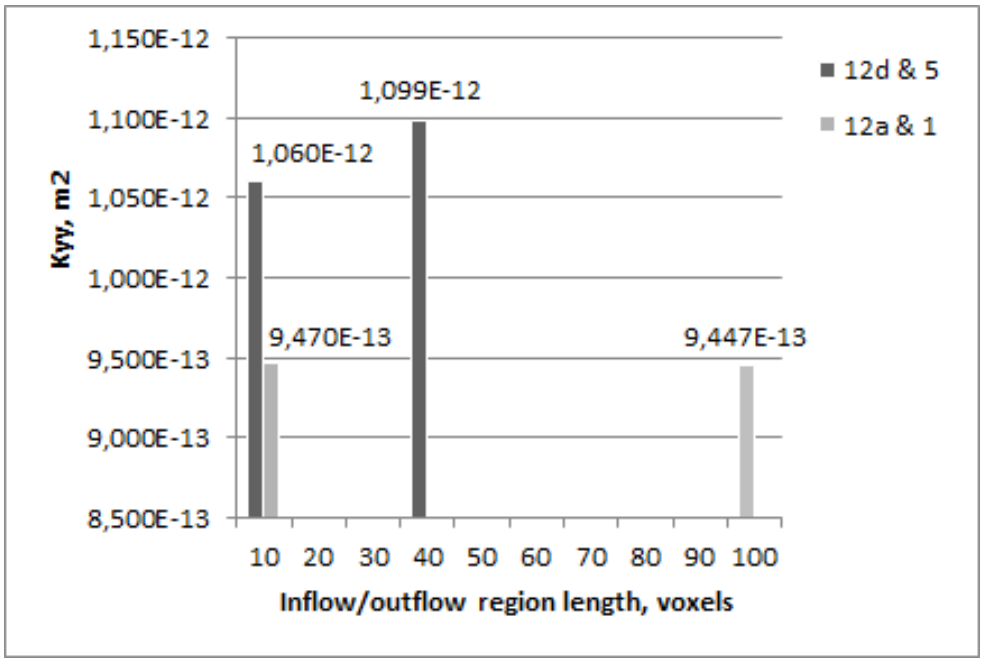

Figure 2: Axial permeability K_{yy} values calculated by the same methods and different inflow/outflow regions for boundary conditions in flow direction

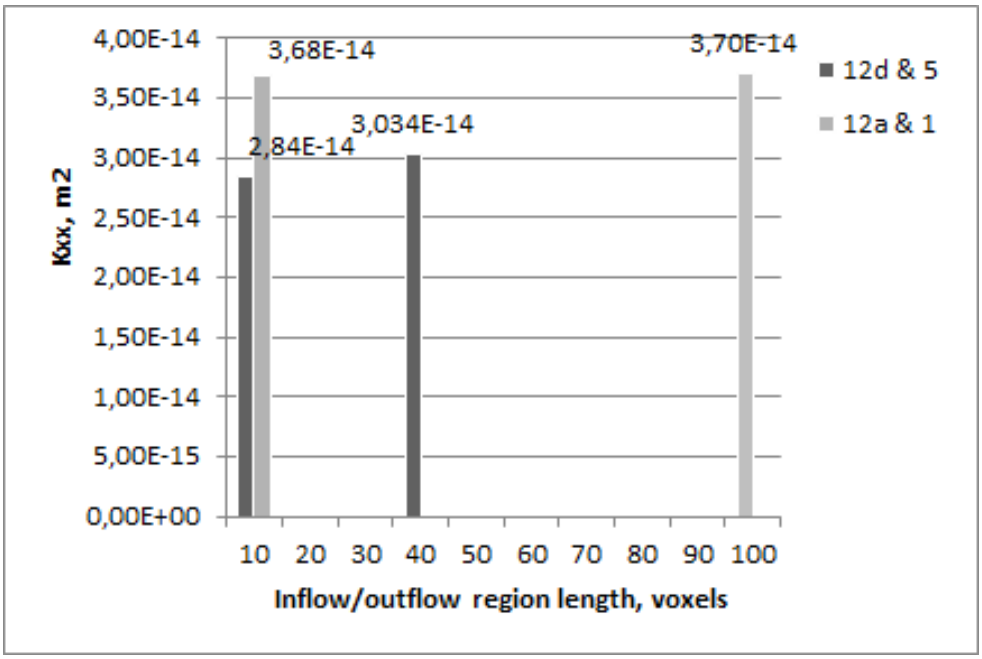

Figure 3: Transverse permeability K_{xx} values calculated by the same methods and different inflow/outflow regions for boundary conditions in flow direction

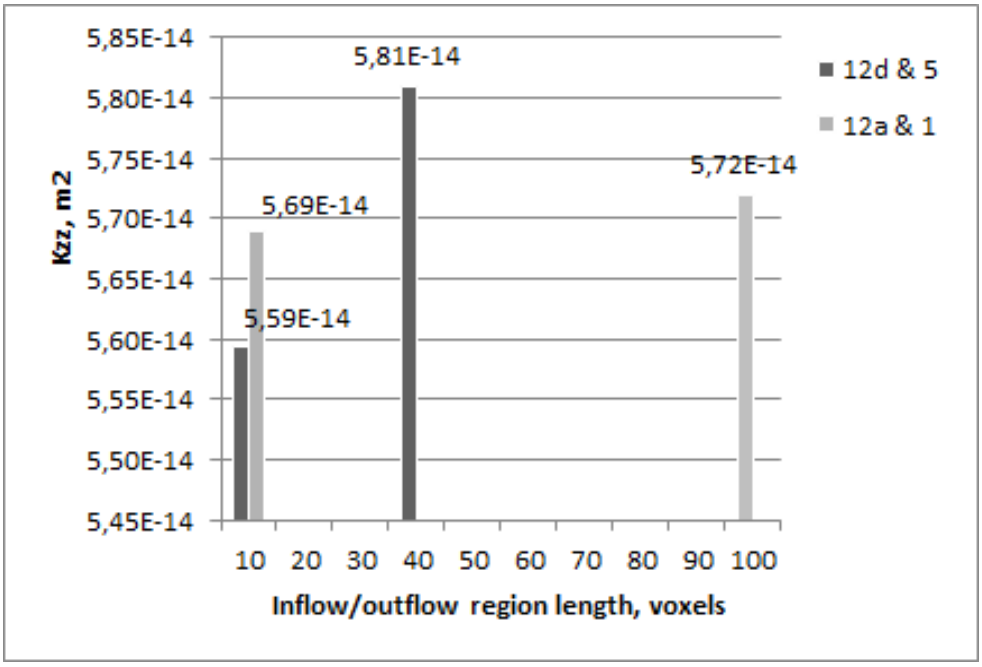

Figure 4: Transverse permeability K_{zz} values calculated by the same methods and different inflow/outflow regions for boundary conditions in flow direction

4 Analysis of the full permeability tensor

Table 3 lists the results that calculated the full permeability tensor, without previously excluded ones.

Table 3: Permeability full tensor results

Participant #	2D / 3D	Permeability tensor, m^2			Permeability determination technique
1	3D	3,70E-14 3,47E-15 8,66E-16	2,87E-15 9,45E-13 -7,25E-15	6,73E-16 4,56E-15 5,72E-14	with Darcy's law accounting for the cross-flows
3	3D	3,34E-14 -2,03E-16 -1,02E-15	2,40E-15 8,42E-13 -9,79E-15	-1,08E-14 -5,87E-15 5,30E-14	with Darcy's law accounting for the cross-flows
5	3D	3,03E-14 2,09E-16 3,99E-18	-7,54E-14 1,10E-12 -1,87E-16	1,01E-15 -2,25E-14 5,81E-14	with Darcy's law accounting for the cross-flows
10b	3D	1,65E-14 5,36E-15 2,28E-15	5,36E-15 8,58E-13 1,74E-14	2,28E-15 1,74E-14 1,02E-14	full-field homogenization
12a	3D	3,68E-14 3,62E-15 8,46E-16	2,85E-15 9,47E-13 -8,02E-15	1,40E-15 -7,26E-15 5,69E-14	with Darcy's law accounting for the cross-flows
12b	3D	2,81E-14 3,27E-19 -4,36E-18	-2,80E-15 1,03E-12 -1,14E-16	4,51E-17 7,47E-17 5,49E-14	with Darcy's law accounting for the cross-flows
12c	3D	3,73E-14 3,66E-15 1,11E-16	3,13E-15 9,71E-13 -1,03E-15	1,15E-14 -5,80E-14 5,79E-14	with Darcy's law accounting for the cross-flows
12d	3D	2,84E-14 5,07E-18 1,44E-19	-2,04E-15 1,06E-12 -1,56E-17	-6,58E-15 -4,72E-15 5,59E-14	with Darcy's law accounting for the cross-flows
15a	3D	2,29E-14 1,90E-15 -5,00E-15	1,90E-15 5,84E-13 -5,30E-15	-5,00E-15 -5,30E-15 3,71E-14	with Darcy's law accounting for the cross-flows
16f	3D	3,93E-14 4,45E-15 1,29E-16	2,66E-15 9,77E-13 -1,05E-15	1,13E-14 -5,85E-14 5,81E-14	with Darcy's law accounting for the cross-flows
16g	3D	4,22E-14 5,07E-15 1,43E-16	1,95E-15 9,88E-13 -1,10E-15	1,07E-14 -5,91E-14 5,85E-14	with Darcy's law accounting for the cross-flows
16h	3D	3,92E-14 4,40E-15 1,25E-16	2,65E-15 9,68E-13 -1,06E-15	1,13E-14 -5,80E-14 5,80E-14	with Darcy's law accounting for the cross-flows
16i	3D	3,68E-14 3,60E-15 8,51E-16	2,85E-15 9,46E-13 -8,02E-15	1,38E-15 -7,17E-15 5,70E-14	with Darcy's law accounting for the cross-flows
16j	3D	3,69E-14 3,59E-15 8,63E-16	2,82E-15 9,43E-13 -8,02E-15	1,36E-15 -7,04E-15 5,70E-14	with Darcy's law accounting for the cross-flows
16k	3D	3,68E-14 3,61E-15 8,49E-16	2,85E-15 9,47E-13 -8,02E-15	1,39E-15 -7,20E-15 5,70E-14	with Darcy's law accounting for the cross-flows
2a, 2b	2D	9,64E-14 -8,96E-16	-8,96E-16 1,26E-13	7,61E-14 -1,53E-15	-1,53E-15 1,01E-13	with Darcy's law accounting for the cross-flows
6b, 6c	2D	1,70E-13 1,30E-15	-2,50E-15 2,51E-13	1,70E-13 -6,01E-16	-6,01E-16 2,51E-13	with Darcy's law accounting for the cross-flows

5 Results based on idealized microstructure

In this section the possibility to approximate the real fiber bundle microstructure by a simplified one, but at the same time the one that should own sufficiently close to the initial structure permeability values, is discussed.

5.1 Analytical predictions

Several participants of the benchmark additionally employed the known analytical models [25-27], often used for the estimation of permeability of yarns at micro-scale. The result #7b corresponds to the assumption of hexagonal arrangement of fibers within the yarn (Fig. 5) by Gebart's model [25] that was developed based on the lubrication theory assumptions. The fibers diameter was taken as an average from the reported for the benchmark sample range of diameters (7.5 - 9.3 µm), i.e. 8.4 µm. Even if the fiber volume fraction varies locally within the tow sample, an average value of 56.5% was taken. The same average FVC was taken in #4b and #4c, but the diameter of 9 µm that is closer to the maximum value of the range was used. The result #4b was obtained by the Gebart's model for quadratic arrangement of fibers, while #4c – for triangular arrangement of fibers studied in [26]. The choice of these two types of fiber packing (Fig. 5) for estimation in #4b,c was motivated by the range of the locally varying within the sample FVC around 56.5%, for which the probability density functions related to these packings of fibers with 3 and 4 nearest neighbors seemed to be the most appropriate (see Fig. 4 in [26]).

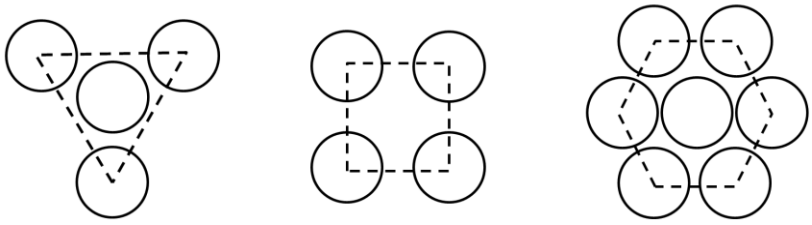

Figure 5: Idealized types of fiber packing assumed in analytical models: a) triangular; b) quadratic; c) hexagonal

As can be seen from the comparison of all results (except the eliminated ones #7a, #11, #13 and #16b), with the analytical estimations (Fig. 6), the latter do not lie within the main cluster of results neither in the case of transverse permeability, nor in the case of axial permeability. The first strong assumption of the analytical models is that the fibers are perfectly straight and aligned, while the fibers within the tow sample of the benchmark are twisted. Due to this, not all fibers of the sample cross its whole length: some of them on the boundaries are present only on a part of the sample.

Secondly, as opposed to the regular arrangement of fibers supposed in analytical models, the fibers within the tow are distributed non-uniformly. The importance of accounting for the non-uniformity of fibers distribution in the model has already been underlined e.g. in [12,35]. As known from the previous studies [26,35,36], at equal fiber volume fraction a non-uniform distribution of fibers within the bundle leads to higher values of axial permeability compared to a regular uniform fibers arrangement, because in axial flow the permeability is dominated by the regions with locally low FVC. This is what can be observed for almost all reported values of axial permeability of the benchmark sample compared to the analytical values (Fig. 6). Only the results #15a, #16l,m,n are not bounded by these analytical values as a lower bound. Results #16l,m,n correspond to the sub-volumes with a different FVC of 58-59%. Results #8a,b are also quite low and, thus, are close to the analytical bound probably due to the high number of introduced in the computation by cropping boundaries (648 sub-volumes).

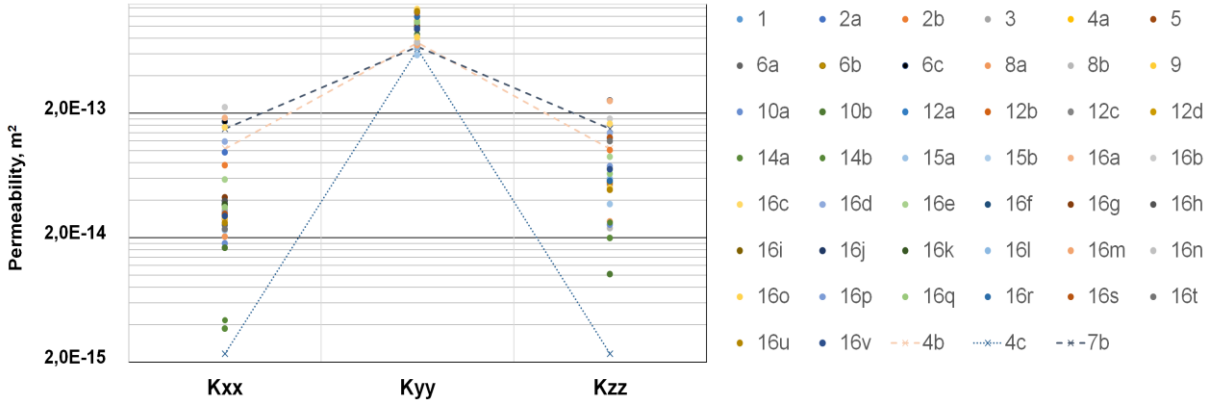

Figure 6: Comparison of the numerical results to the analytical predictions #4b, #4c, #7b with the assumptions of quadratic, triangular, and hexagonal fiber arrangement, respectively

On the other hand, the transverse to fibers permeability is dominated, vice versa, by the regions with high density of fibers [35,37,38]. Therefore, a non-uniform distribution should lead to lower permeability compared to a regular arrangement. In Fig. 6 it can be seen that the large majority of values of transverse permeability are “bounded” from an upper end by the analytical values, namely, the ones corresponding to the Gebart’s model with quadratic and hexagonal packing. However, the results #16a-d, as well as #6b,c are situated above this bound. Results #16a-d were obtained by the explicit-jump immersed interface method [22], known to be not adapted to the low-porous structures, by varying residual tolerances and boundary conditions. One should note that other results obtained also by the EJ method #16e,l-v, but with a smaller tolerance, are situated on the other side of the analytical values, i.e. below them. Results #6b,c were calculated from 2D simulations by

averaging the pressure/velocity fields for Darcy's law accounting for the cross-flows, that are not accounted for in #6a.

The same relative position of the computed axial and transverse permeabilities with respect to the analytically predicted ones was observed for other FVC in the values computed on 10 sub-volumes in #4 (Fig. 7).

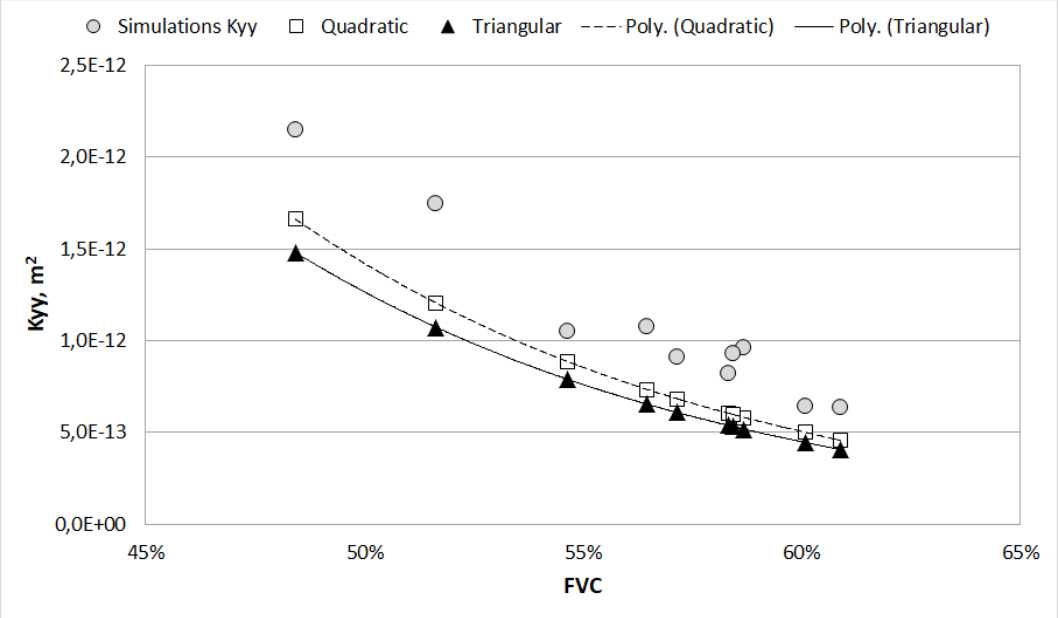

a)

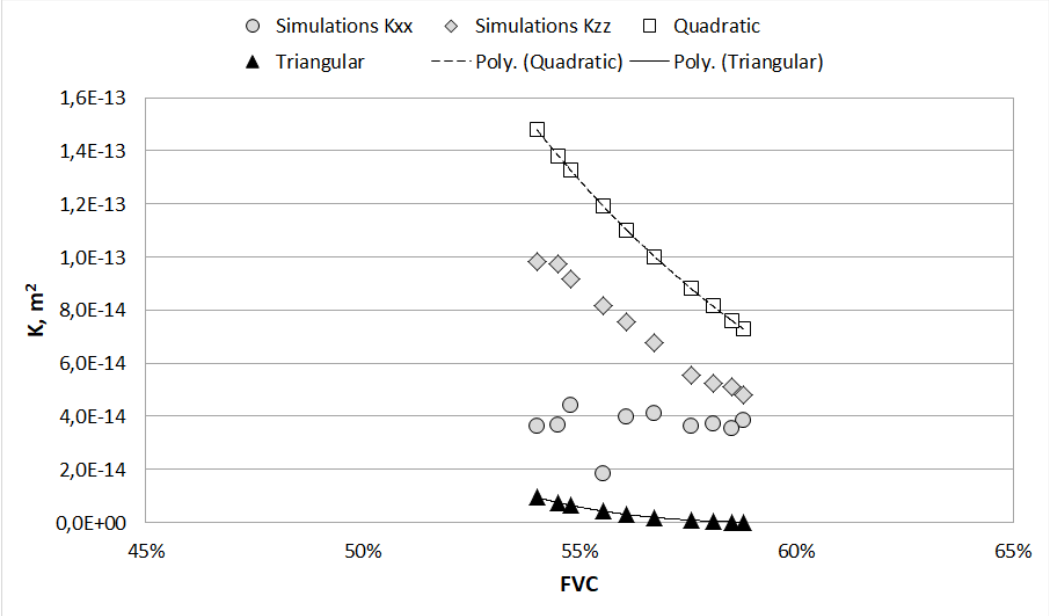

b)

Figure 7: Comparison on 10 sub-volumes of the numerical results #4 and analytically predicted values with the corresponding FVC, fibers diameter of 9 µm, and assumptions of quadratic [25] or triangular [26] fiber packing

As shown, the deviation between the analytical prediction and the computed fiber bundle permeability can be very significant, especially in case of transverse permeability. In addition

to the listed above differences with the idealized structure, there is also a variation of fiber diameters within the sample.

5.2 Numerical predictions on a virtually generated microstructure

Different ways to replace a real fibrous microstructure by a simplified one might be of interest when a complete 3D information about the structure at such a fine scale is not accessible, e.g. there is no possibility to use the X-ray computed tomography etc. If only 2D image data are available (e.g. from an optical microscope), one possible way out is to make an extrusion of a transverse cross-section of the fiber bundle. This approach was followed by the benchmark participant #11 (though motivated by computational reasoning): the front cross-section of the 3D sample corresponding to the 59% FVC was extruded to obtain a new 3D volume. It would be interesting to quantify the impact of the extruded structure, and, hence, the fibers misalignment on the permeability. However, it was not possible to do based on the unrealistically high values #11 due to the scaling problem already explained in Section 4.2. It should also be noted that the use of the extrusion approach on the benchmark sample would not allow to isolate the effect of only fibers misalignment but would also include the effect of the fiber volume fraction since it varies along the fibers within the sample.

Another way to use a simplified microstructure in the computation is to virtually generate it by preserving the key geometric parameters that are important from the permeability perspective: fibers dimensions, FVC, fibers arrangement within the tow. The result #15b was computed on a fiber bundle (Fig. 8) created by a virtual microstructure generator, which is based on the random sequential addition method [39-40]. By prescribing a constant fiber diameter of 9 μm, the fiber volume fraction of 51%, and the normal distribution of random fiber locations, 268 aligned fibers were generated within this virtual sample keeping the same dimensions as in the benchmark sample.

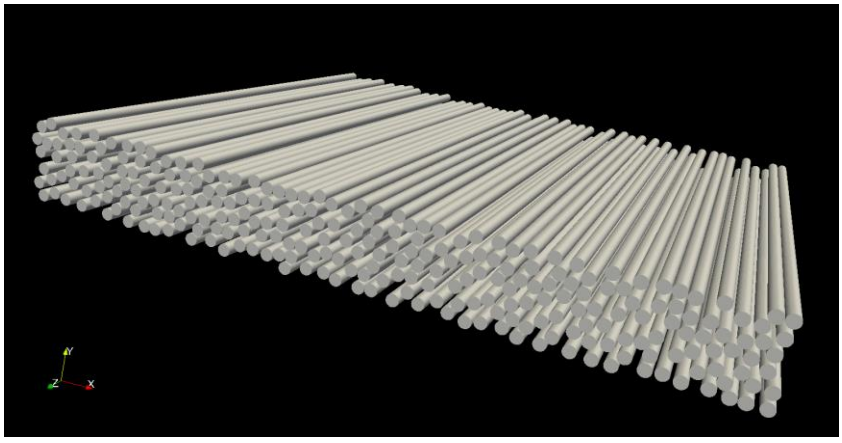

Figure 8: Virtually generated microstructure at 51% FVC with aligned randomly distributed fibers of equal diameter

The relative difference between the values #15b and #15a obtained by the same method on the virtual microstructure at 51% FVC and the real one at 56.46% FVC respectively, is 69% for the transverse permeability and 40% for the axial one. A smaller deviation would be achievable with the replication of the same FVC, and introduction of the varying fiber diameters as in the real microstructure, whereas the fibers misalignment is more complex to address.

The question of substituting the real fibrous structure by a virtually generated one needs to be further investigated to define which geometrical parameters must be reproduced in the virtual microstructure, and which can be neglected in the model.